*Fatigue & Fracture of Engineering Materials & Structures*

WILEY

FFEMS Fatigue & Fracture of Engineering Materials & Structures

SPECIAL ISSUE ARTICLE OPEN ACCESS

# Fracture Analysis of 316L Specimens Fabricated via Material Extrusion Additive Manufacturing: Influence of Building Orientation and Notch Acuity

Saveria Spiller | Sara Couto | Nima Razavi

Department of Mechanical and Industrial Engineering, Norwegian University of Science and Technology, Trondheim, Norway

**Correspondence:** Nima Razavi (nima.razavi@ntnu.no)

**Received:** 15 May 2024 | **Revised:** 2 September 2024 | **Accepted:** 20 September 2024

**Keywords:** fracture | material extrusion additive manufacturing | porosity | steel | three-point bending test

## ABSTRACT

Three-point bending tests were performed on notched specimens extracted from cuboids of 316L stainless steel produced via material extrusion additive manufacturing. The cuboids were printed vertically and horizontally on the printing platform to account for the building orientation effect on the mechanical performance. For each orientation, three notch sizes were considered. Overall, the specimens printed with building direction parallel to the loading direction outperformed the others. A significant notch size effect was observed in these specimens since the sharpest notch provoked a decrease in the peak load reached by the specimens in comparison with larger notches. On the contrary, this effect was less relevant among the other specimens, which presented a conspicuous amount of residual porosity that contributed to the premature failure. Further investigations were carried out to correlate the building orientation to the density of the parts and, ultimately, to the investigated mechanical properties. The ASED and TCD criteria were also applied to assess their accuracy in the failure prediction of the tested specimens.

## 1 | Introduction

The interest of the scientific community in additive manufacturing (AM) has been a rising trend that has not slowed down in decades, developing technologies that are more accessible and consolidated every day [1]. Numerous studies and reviews analyzed the challenges and benefits of AM over traditional subtractive processes, contributing to several fields such as aerospace, medical and healthcare, automotive, and architecture [2]. AM allows the creation of parts on demand, reducing the need for stocking; it also enables the production of lightweight components, and the material waste through the process is limited [3]. For these reasons, AM is claimed to be sustainable, which is a paramount topic in our era. The design freedom and customization options promote the development of many different processes and hybrid technologies, and the field is rapidly broadening.

In 2020, the metal AM market was taken for 54% by powder bed fusion (PBF) techniques, followed by directed energy deposition and metal binder jetting [4]. Material extrusion additive manufacturing (MEAM) occupies only 10% of the market. According to ASTM 52900 [5], the term *material extrusion* describes the family of techniques in which the feedstock material is selectively dispensed through an orifice or nozzle. This technique has been widely used for the fabrication of components using filaments or pallets of a wide range of polymers or reinforced polymers [6]. However, it is possible to obtain metal parts using a filament composed of a mixture of polymeric binder and metal powder. Some companies have already produced polymeric filaments with small amounts of metal powder to give a metallic appearance to the printed parts [7, 8]. Commonly, when utilizing the MEAM process for the fabrication of metallic components, the feedstock has a metal powder infill percentage of at least 60 vol%, and it is referred to as a high-infill polymer (HP) [9].

**Summary**

- Notch fracture was assessed on MEAM 316 specimens of various notch geometries.
- Building orientation effect on the porosity, mechanical response, and failure mechanisms was investigated.
- The numerical tools ASED and TCD provided a good engineering estimation of fracture.


The result of the printing step is an intermediate product called the *green part*, from which the polymer must be removed. This is achieved in a process called debinding, the result of which is called *brown part*, and consists of packed metal powder. The shape retention of the brown part is guaranteed by the high percentage of metal powder in the feedstock material. Finally, the brown part is sintered at a high temperature in a controlled atmosphere, to allow the diffusion of the metal powder and the densification of the part. Unless post processes are needed to increase the parts' quality, sintering is the final stage of the process, whose outcome is usually referred to as the *silver part* [9, 10]. Figure 1 represents a schematic of the process. The two magnified details of a layer's interface show the difference in the material composition before and after debinding and sintering have been performed.

The present work is focused on the bending behavior of 316L stainless-steel notched components extracted from bulk parts obtained via MEAM. The main investigation is related to the notch size effect in the behavior of specimens tested in three-point bending conditions (3PB); therefore, notches with different tip radii are machined in the specimens. Notches are geometrical discontinuities that are studied to ideally represent the reality of mechanical parts and load-bearing components, whose stress fields are altered in the presence of geometrical defects or functional design features. For a comprehensive understanding of the topic, two sets of specimens were tested, with identical designs and notch geometries but printed in different orientations. This is a necessity since the effect of the building orientation on MEAM parts was proven to be significant: multiple works available in the literature studied the effect of the building orientation on the tensile properties of stainless steel, specifically 316L and 17-4 PH, revealing that the parallelism of loading direction and building direction is the least favorable condition in terms of strength and elongation [12–17]. This is mainly attributed to the poor adhesion of the layer's interfaces that are likely to delaminate provoking failure. The building direction was proven to also affect the flexural behavior of components produced with this technique. Some examples of rectangular stainless-steel specimens printed in two orientations, flat (i.e., printed along the thickness) and on the edge (i.e., printed along the width), tested in 3PB conditions can be found in [18–20]. In these examples, the difference between the average strength in the two orientations is relatively small, while the dispersion of the data is relatively high. Consequently, it is not possible to strongly state that one direction is better than the other. This conclusion is also corroborated by what was obtained in [21] by Thompson et al.: In their work, a significant scatter among 3PB results was observed, although the specimens were supposed to be identical, and the authors attributed that effect to the intrinsic instability of the MEAM process. Every phase involves many parameters, and their definition is not a sufficient condition to guarantee the same density and porosity distributions in ideally identical parts. With the development of this concept, a possible beneficial effect obtained from a wise choice of the building orientation of a part might be nullified by the presence of a localized random defect originating in the fabrication process.

An antithetical conclusion is obtained by Carminati et al. [22]. In their work, MEAM is claimed to be a repeatable process since the 3PB test results obtained in their study present minimal scatter. According to the authors, the reason is the limited gauge area in a 3PB specimen, which reduces the probability of finding one of the abovementioned random defects in the most stressed area of the specimen.

Besides the building orientation, it is claimed in several works that other printing parameters do not affect the bending behavior of the parts. For example, in [23], 3PB specimens were printed with different infill density percentages: The parameter was finally proven to have a nonsignificant impact on the results. In the study by Kesha et al. that was previously mentioned [20], for each printing orientation, the raster angle of the rectilinear infill and the layer height were also changed. The bending tests revealed a minimal impact of these parameters on the properties of the specimens. Similarly, in [18], it is reported that the effect of printing speed and layer height is limited, although it is suggested that thicker layer heights might be beneficial since in this way the number of weak interfaces in the part is reduced. Each of the works mentioned above was carried out on unnotched specimens. To the best of the author's knowledge, single-edge notch bars produced by MEAM were used to perform only Charpy impact tests [22, 24], but the effect of the notch size and the building

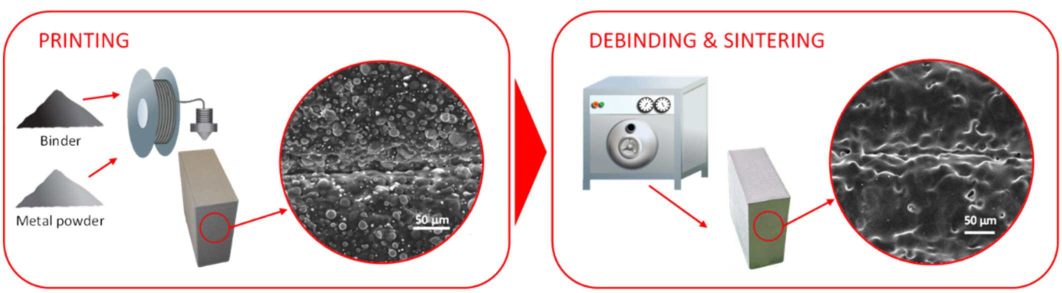


**FIGURE 1** | Schematic of the process of material extrusion additive manufacturing with magnifications of a layer's interface appearance before and after debinding and sintering. On the left, metal powder particles are visible in the polymeric matrix, while, on the right, the material is homogeneous. The picture is redrawn from [11]. [Colour figure can be viewed at wileyonlinelibrary.com]

orientation on the mechanical behavior of notched specimens tested in a 3PB configuration has not been investigated yet.

A secondary research question addressed in the present work is related to the predictability of the failure load of the 3PB notched specimens via theoretical criteria. Some established theoretical tools such as ASED (average strain energy density) and TCD (theory of critical distance) have been already widely used in similar experimental campaigns. There are other possible methods to predict failure conditions; some examples, listed in [25], are the J-integral criterion, the cohesive zone model (CZM), the finite fracture mechanics concept (FFM), and the theories of gradient mechanics (GE) [26, 27]. In this scenario, TCD and ASED present the undeniable advantage of their simplicity. They are based on the postprocessing of stress fields obtained via uncomplicated linear elastic FE models, and they require the knowledge of a limited number of parameters. Moreover, the ASED criterion was proven to be mesh independent, further simplifying the FE model. For a more detailed discussion about the convenience of these methods, the reader is referred to [28–30].

Both the TCD and the ASED criteria can be used to predict the failure conditions of specimens affected by stress risers in static and fatigue loading. Theoretically, the methods shall be applied to homogeneous, isotropic, and linear elastic materials. Nonetheless, several examples available in the literature report successful prediction on materials that do not meet these requirements. For example, the methods have been applied multiple times to AM parts, intrinsically nonisotropic [26, 31–37]. To overcome the requirement about the linearity of the material constitutive law, it must be noted that several methods exist to reduce the real material to an equivalent homogeneous and brittle material [31, 32]. Nonetheless, TCD was successfully used on ductile materials without taking advantage of those strategies [28, 38, 39].

As regards the homogeneity of the materials, it can be argued that the AM parts are heterogeneous not only for the layer-by-layer building strategy but also for the extensive distribution of defects and residual porosity that are typically process induced. Neither of the two methods, TCD and ASED, directly consider the defects in the materials. To overcome this issue, micromechanistic approaches that fall outside the scope of the present work must be considered [40, 41].

To briefly describe the methods, ASED is a local approach, formulated in [42], that was first applied to V-notches and then extended to U-notches in [43]. According to the criterion, the failure of notched specimens occurs when the strain energy density averaged on a circular control volume around the notch tip reaches a critical value. Both critical value and control volume are considered material-dependent properties. The TCD is a family of different methods, among which the point method (PM) is the simplest. Instead of defining a circular control volume, TCD defines a length parameter $L_c$, which is also claimed to be a material property. According to the PM, failure occurs when the maximum principal stress reaches a critical value at a distance of $L_c/2$ from the notch tip. The critical strength is referred to as inherent material strength [44], which for brittle materials coincides with the material's ultimate tensile strength. Some extensions of the TCD are named line methods and area methods, which consider the stress as an average over a line or an area, respectively, whose characteristic length is always $L_c$. All the material parameters mentioned in this paragraph will be obtained through a calibration procedure, since to the best of the author's knowledge, no available data on 316L SS MEAM parts is available.

The work is structured as follows. Section 2 reports the description of the fabrication process, the specifications of the lab equipment used, and the numerical models implemented. Section 3 collects the results of the performed tests with several subsections including one dedicated to a fractographic study of the fracture surfaces of some selected specimens (Section 3.4). Section 3.5 describes the numerical models and procedures used to demonstrate the predictability of the failure conditions of the tests via the theoretical methods ASED and TCD. Some final remarks and useful indications for future works are reported in Section 4, along with suggestions for possible design solutions.

## 2 | Materials and Methods

### 2.1 | Specimens' Fabrication

The fabrication of the parts was carried out using an FDM Prusa printer i3 MK3S and the commercial filament BASF Ultrafuse 316L, which contains $>80$ wt% of 316L metal powder with an equivalent diameter ranging from 4 to 40 μm [11]. The high solid infill percentage entails several challenges in the extrusion and deposition processes. The metal powder increases the viscosity of the compound, undermining the stability of the flow of the softened material. Moreover, the heat transmission of the metal powder–polymer composite results in rapid hardening and hinders the adhesion of the deposited material, inducing major defects such as warping, delamination of the part, poor shape retention, and lack of extruded material (underextrusion). To avoid these issues, the printing parameters must be carefully chosen. A tuning process is often necessary since the printing procedure is strongly dependent on the printer and the type of material used.

In the present work, specimens in the shape of cuboids were designed with dimensions of $30 \times 28 \times 15$ mm. The models were scaled up to be able to compensate for the shrinkage that occurs during the sintering process. From other studies, the overdimensioning factors were defined as 19% and 21%, respectively, on the $x$–$y$ plane and along the $z$-axis. The shrinkage is more significant along the building direction of the part ($z$-axis) because the removal of the binders leaves elongated voids along the layers' interfaces; therefore, the layers tend to collapse on top of each other, making the size reduction more visible. The cuboids were printed in two orientations, flat on the printing platform and vertically, using the same set of printing parameters. Some of the more important are the following: extrusion temperature 290°C, printing platform temperature 110°C, layer thickness 0.1 mm, nozzle diameter 0.4 mm, flow rate multiplier (FRM) 100%, and cooling fan speed 50%. The high extrusion temperature is required to overcome the issues previously described, such as the brittleness and viscosity of the filament. The layer thickness and the nozzle diameter were considered appropriate to ensure the accuracy of the printed parts, to the cost of a reasonable reduction of the printing duration. To avoid the underextrusion issue, it was thought to increase the FRM, which is the indicator of how much material is pushed through the nozzle, but the obtained results were poor in terms of surface quality and smoothness of the sides. For this reason, after several attempts, it was chosen to keep the FRM at the default value (100%). As regards the cooling fan speed, it was observed that the material solidification rate was high, hindering the adhesion of the layers. It was not necessary to keep the cooling fan at the maximum capability throughout the printing; hence, they were set at 50%. To further promote the adhesion of the first layer to the printing platform, the cooling fan was completely off exclusively during the deposition of the first layer. Further details regarding the impact of process parameters on the printing outcome can be found in [45, 46]. The first layer of a part is always the most critical; therefore, other strategies were implemented to avoid printing fails, for example, the addition of a large brim, the increase of the first layer thickness from 0.1 to 0.15 mm, and the increase of the platform temperature. The green parts obtained were outsourced for debinding and sintering to an appointed company, Elnik Systems GmbH. The debinding was carried out at 120°C in $HNO_3$ atmosphere, while the sintering process reached a maximum temperature of 1380°C held for 3 h. The silver parts were measured with a caliper to evaluate the actual shrinkage after the process. Afterward, the cuboids were machined to extract the specimens using an EDM wire cutter machine.

## 2.2 | Experimental Procedures

Microstructure analysis and Vickers microhardness tests were performed on sections extracted from each cuboid that were cut and embedded in hot resin to be ground and polished up to 1-μm scratch size. The sections were etched using the V2A reagent, composed of 10 mL of $H_2O$, 10 mL of HCl, and 1 mL of $HNO_3$, to expose the general structure of the grains. This etchant was previously proven to be effective on 316L stainless steel [11]. The microhardness tests were conducted with the Mitutoyo hardness machine MicroWidZhard HM-200 series, provided with a diamond indenter. Several indentations with a force of 0.2 kgf were made to capture possible hardness trends through the thickness and width of the cuboids.

As depicted in Figure 2a, single-edge notched specimens were extracted from one vertical and one horizontal cuboid, with notch radii of 0.25, 0.5, and 1 mm, following a specific sequence. In this figure, the appearance of the different notch sizes is shown (Figure 2b), as well as the most relevant dimensions of the specimens inside the three-point bending fixture that was used for the 3PB tests (Figure 2c). To avoid misunderstanding, a specific nomenclature has been designed to identify the different specimens. For the sake of simplicity, the two cuboids are called horizontal (H) and vertical (V), and, for extension, the specimens extracted will be also referred to as *horizontal* and *vertical* specimens, when further specifications are not required. As shown in the figure, both cuboids were first cut parallel to the longest dimension obtaining two sections per cuboid that were finally cut into rectangular specimens. To distinguish the position of the rectangular specimens, the sections are called horizontal top (HT), horizontal bottom (HB), vertical right (VR), and vertical left (VL). Finally, the notches were cut from every rectangular specimen, with alternating notch radius in an ascending sequence: 0.25, 0.5, and 1 mm. Therefore, for each section of HT, HB, VR, and VL, there are multiple specimens with the same notch size, which are distinguished by reporting the Roman number in brackets. For example, the nomenclature HT-0.5(I) refers to the first specimen with a 0.5-mm notch radius extracted from the top section of the horizontal cuboid.

The tests were performed in a STEP Lab UD020 testing machine with a 20-kN load cell, in the 3PB fixture depicted in Figure 2c. The bending tests were carried out with a displacement rate of 1 mm/min. The tests stopped automatically after reaching a preset displacement value to prevent damage to the fixture and the machine. Digital image correlation (DIC) was also used to extract further information from the test, such as the notch opening displacement. Appendix II reports also two examples of strain fields derived from the DIC analyses. The DIC technique is based on the acquisition of time-interval pictures of the specimen during the test. The specimens are painted on a white homogeneous background with a black speckle pattern on top. The black speckles are obtained using a spray can paint, to obtain spherical fine drops with a random size distribution. Fine speckle patterns are desirable since they ensure more accuracy, although this comes at the cost of readability. Due to the size of the specimens, it was challenging to find a trade-off, and the finest pattern possible was painted. It must be noted that the main goal of the DIC analysis was to evaluate the mouth opening displacement of the notches, which is of macroscopical scale. This was necessary since the specimens were too small to allocate an extensimeter. The pictures (with a resolution of $2452 \times 2056$ and a pixel size of approximately $3 \times 10^{-2}$ mm) were taken with a camera connected to the acquisition software VIC-Snap, and the analyses were then performed in the software VIC-2D.

Although for the bending test, no surface preparation was needed, some specimens were ground and polished to allow a qualitative evaluation of the porosity using the optical microscope, Hirox RH-2000. Two specimens with 0.25-mm notch radius, vertical and horizontal, were ground up to 4000 grit and then gently polished with a 3-μm–scratch size cloth, using diamond polishing suspension. Finally, the fracture surfaces were exposed and studied with the SEM microscope FEI Quanta 650 FEG and the confocal microscope Alicona G4 IFM.

Moreover, some dog bone specimens were extracted to evaluate the tensile properties of the material in both orientations, to be able to provide the FE software Abaqus with a suitable material model and to predict the failure load of the 3PB specimens using predictive numerical tools. The tensile tests were performed on the universal machine MTS Criterion Model 42, provided with a 5-kN load cell, with a displacement rate of 1 mm/min. The deformation of the specimens was calculated using the DIC.

## 2.3 | Numerical Procedure and Theoretical Background

The application of the ASED and TCD criteria requires the preparation of 2D models of the notched specimens in a 3PB configuration. Since the criteria were originally formulated for linear

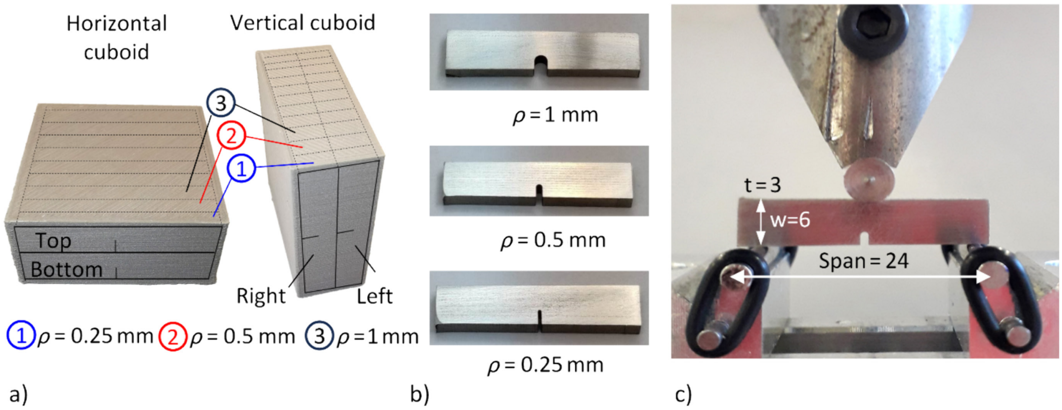


**FIGURE 2** | (a) The specimen extraction overview. The order of extraction is 0.25-, 0.5-, and 1-mm notch radii, and the sequence is repeated throughout the cuboid; (b) representative test specimens of different notch geometries; (c) three-point bending test configuration. Dimensions in millimeters. [Colour figure can be viewed at wileyonlinelibrary.com]

elastic materials, a linear elastic model is used in the present work to ideally represent the behavior of the material. The plastic behavior of 316L stainless steel is relevant; hence, reducing it to a linear material introduces significant approximations. Nonetheless, there are reasonable reasons to attempt the application of the linear elastic fracture mechanics (LEFM) approach to predict the static failure of the 316L bending specimens. For one side, LEFM is chosen for convenience since simple models and very short computational time are desired characteristics in a numerical study. On the other side, such an approximation is legitimized by examples of research such as the work of Susmel and Taylor [28], which applied TCD using both linear and elastoplastic models to predict the static failure of notched steel components. Interestingly, the accuracy of the linear elastic prediction is as acceptable as the elastoplastic analyses. In light of this, the first models prepared in the present work consider a material with a linear elastic constitutive law, which requires knowing only Young's modulus and Poisson's ratio. The FE software Abaqus with the standard model was used, and the 2D models were prepared using the dimensions of the actual specimens. The 3PB configuration is obtained by setting suitable boundary conditions on the displacement of the lower supports and a concentrated force on the upper edge on the symmetry axes of the specimen. The mesh is composed of plain strain CPE8R elements. Partitions are used to help the smoothness of the mesh and hence increase its quality. The size of the elements is gradually decreasing towards the notch tip until convergence, with a nominal minimum value of 0.01 mm. It should be noted that a mesh sensitivity analysis is required to correctly calibrate the TCD. On the contrary, ASED is relatively independent by the mesh size [47].

The detailed procedure to apply ASED and TCD criteria is presented in Appendix I. In a nutshell, ASED allows the prediction of the failure load $P_f$ of a specimen according to the equation $P_f = P\sqrt{W_C / \overline{W}}$, where $\overline{W}$ is the average strain density calculated for a reference model implemented in the FE software with a known applied load $P$. $W_c$ is the critical value of the strain energy density, usually calculated as $W_c = \sigma_t^2 / 2E$. The value $\sigma_t$ is the tensile strength of a brittle material. When a ductile material is under consideration, the definition of an appropriate $\sigma_t$ is an issue to be addressed. To apply ASED, it is also necessary to calculate the radius of the control volume $R_c$. The definition of $R_c$ depends on the notch geometry and the stress field in the component. The equations used to calculate the $R_c$ of a U-notched specimen in plane stress conditions are also described in Appendix I.

The same 2D models were used to extract the stress distribution in the specimens along the notch bisector in the condition of incipient failure to find the material length scale parameter $L_c$ and apply the TCD. According to the PM, the failure occurs when the maximum principal stress at a distance of $L_c/2$ from the notch tip exceeds the inherent material strength. For ductile material, the $\sigma_t$ might be a good starting value of the inherent strength [39], although the value might require adjustments based on the error between predicted and experimental failure loads.

## 3 | Results and Discussion

### 3.1 | Characterization of the Sintered Cuboids

*Shrinkage*: The sintered cuboids were measured with a digital caliper to calculate the linear reduction percentage in each direction as $(d_g - d_s)/d_g$, where $d_g$ is the green part dimension and $d_s$ is the silver part dimension. Average shrinkage rates of 19% and 22% were obtained along the *x*-/*y*-axis and the *z*-axis (i.e., the printing direction), respectively, for both cuboids, which is in good accordance with what was found in similar works on the same technique and material [11, 48].

*Microstructure*: As previously explained, besides the three-point bending specimens, some sections were extracted from the cuboids for microstructural characterization. Figure 3a shows where these sections were extracted. The sections were mounted in hot resin, ground, and polished following the procedure described in the previous section. The general structure of the crystal lattice was exposed using the V2A etchant. The grains, displayed in Figure 3b, are equiaxial with an average equivalent grain diameter of 44 µm, which is consistent with the reported microstructure in the literature [49, 50]. The observed equiaxed microstructure in these parts results from the sintering process, which differs fundamentally from other AM processes such as

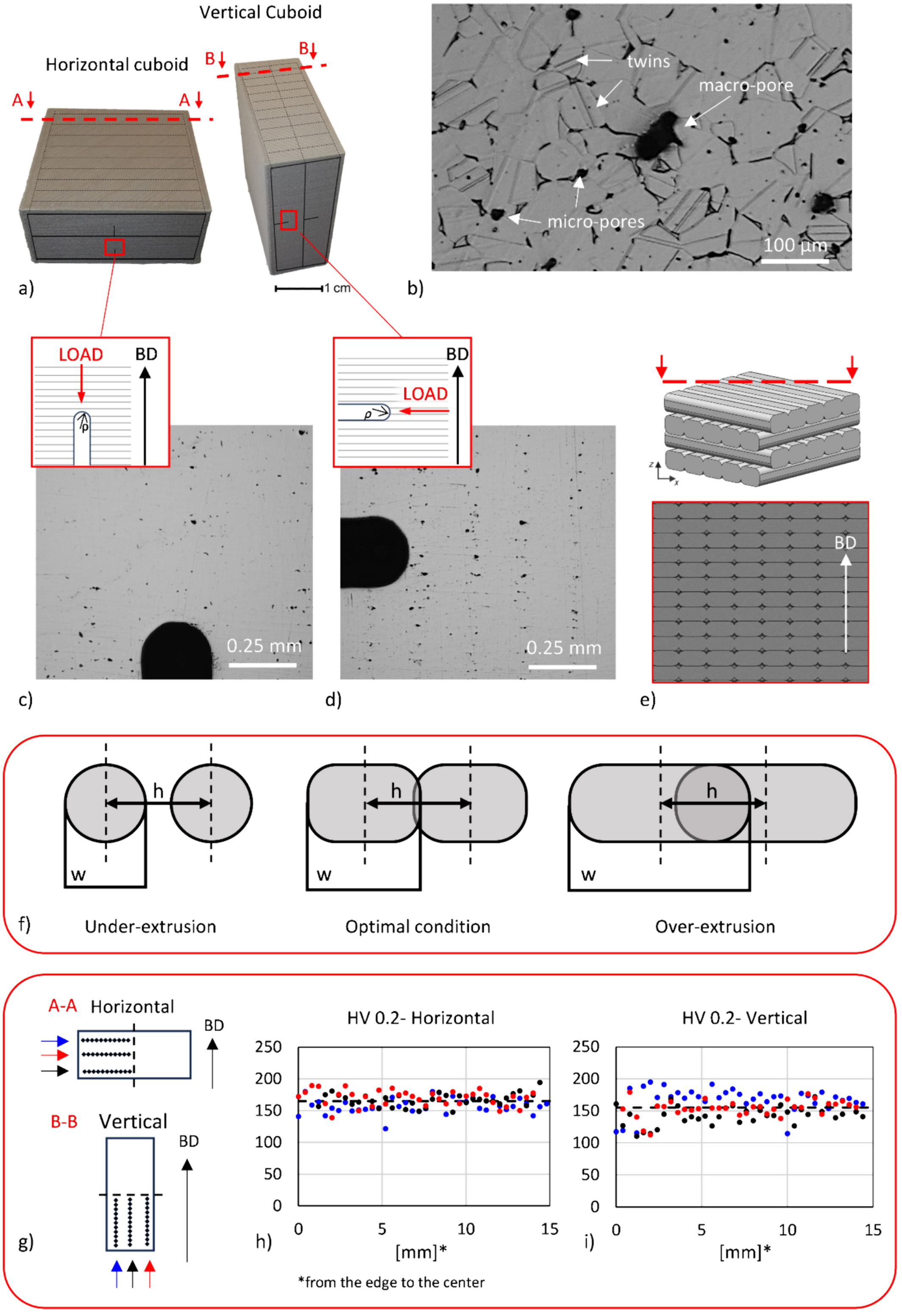


**FIGURE 3** | (a) Schematic of the extraction of the specimens from the cuboids; (b) typical microstructural features obtained from the etched sections; (c, d) magnifications of the area around the notches in the two cuboids, with indications of the building direction (BD) and the load direction; (e) schematic of the printing-originated pore distribution; (f) illustrations of the appearance of the so-called underextrusion and overextrusion defects; (g–i) schematic of the indentations positions to measure the Vickers microhardness and the plots of the data obtained for the horizontal and the vertical samples. Blue, black, and red represent the three lines along which the indentations are taken. [Colour figure can be viewed at wileyonlinelibrary.com]

PBF. In PBF techniques, the high heat sources locally melt the material followed by rapid cooling, which promotes grain elongation along the building orientation (heat dissipation direction), resulting in an anisotropic microstructure [51]. The grain size of sintered parts is in general coarse, depending on the temperature and dwelling time of the sintering process. This is a result of the mass transportation mechanisms that occur across the newly formed grain boundaries, which led to the enlargement of the grains [52]. Several fields per sample were observed with the optical microscope, and consistent microstructure was observed along the thickness and height of the samples. Moreover, due to the isotropic texture, the microstructure observed in the vertical and horizontal samples was identical, as confirmed in other works where it is stated that the building orientation does not affect the microstructure texture [13, 48, 53]. Typical features of sintered austenitic steels are visible, such as twinning planes and microvoids located at the intersections of the grain boundaries. The latter are possibly the result of trapped gas, contained in the powder, which creates pressurized pockets in the matrix, resisting the grain growth. It is claimed that increasing temperature and dwell time of the sintering process could contribute to the further coarsening of the grains without succeeding in reducing the porosity [13, 54]. Besides the microvoids, there is a second type of porosity characterized by larger voids whose size is comparable to the grains' size. This porosity is "process induced" [51], or to be more precise, "printing induced," and its distribution deserves investigation.

*Printing-induced porosity*: Figure 3c,d depicts respectively one horizontal and one vertical specimen with a 0.25-mm notch radius that were ground and polished as described earlier. The horizontal specimen (Figure 3c) does not show any specific porosity pattern. On the contrary, in the vertical specimen (Figure 3d), arrays of voids are visible to the naked eye. The schematic in Figure 3e and the indication of the building direction shall help us understand that the voids do not indicate the layers' interfaces, as a superficial analysis would suggest, but they are located between adjacent *intralayer* rasters (i.e., in the same layer). Conversely, the material between the arrays looks significantly more homogeneous, suggesting a decent *interlayer* adhesion. While the micropores described in the previous paragraph originated in the sintering process [13], the origin of these larger voids occurs during the printing phase. During the deposition, the softened material assumes a deformed shape, as depicted in the schematics in Figure 3f, whose dimensions depend on several printing parameters. For example, it has been proven that the speed of the nozzle affects the quantity of the deposited material and therefore the volume of the pores [55]. Indeed, smaller pores are observed close to the turning points of the nozzle path along the edges of a part, since the nozzle deceleration allows more material to flow. Moreover, at the turning points, the first segment of a raster is deposited immediately after the final part of the previous one, meaning that the material is still warm, and the adhesion is facilitated. In the work of Godec et al. [56], it was also proven that the temperature and the flow rate are important factors in controlling the density of a green part: higher temperature reduces the viscosity of the filament, increasing the flow rate. Proper tuning of these parameters helps to avoid the so-called underextrusion and overextrusion defects, defined in [57] and depicted in the schematic in Figure 3f. In the urge to avoid underextrusion, it might come naturally to excessively increase temperature and flow rate, but the excess material will provoke other typical defects of FDM parts, such as deformation of the bottom layers, poor shape retention on the edges, and enhanced roughness [57].

All the voids created during the printing process experience shrinkage during the sintering process. As already discussed in the previous paragraph, the specimens shrink more along the $z$-axis. This implies that the interlayer voids are more prone to close in comparison with the intralayer ones. The remarkable difference between the porosity in the horizontal and vertical specimens is an issue to be addressed. Damon et al. [13] concluded that not only the infill strategy but also the building orientation strongly affect the morphology and distribution of the porosity. For example, given the same infill strategy adopted in the present work (rectilinear rasters with alternating 45°/−45° angles), specimens printed vertically showed higher porosity than the horizontal ones. In light of the previous considerations, the shape of the cuboids might be the origin of this issue, indeed during the printing phase, it was observed that the vertical cuboids were particularly complicated to print, especially for what concerns the shape retention and the smoothness of the side surfaces. Localized roughness on the sides and underextrusion defects were more likely to appear in comparison to the horizontal cuboids. This effect is probably related to the increasing distance from the hot printing platform while increasing the height of the part, resulting in continuously changing heat conditions. In a previous work performed by the authors, it was also noticed that smaller sections are more prone to be affected by underextrusion defects since the nozzle speed is more unstable. Considering the smaller planar extension of the vertical cuboids, this can also be a reason for the challenging printing procedure [55].

*Microhardness*: The polished sections used for the microstructural evaluation were also used for microhardness tests. Vickers microhardness was assessed following the schematic in Figure 3g, which entails multiple diamond indentations imposed with 0.2 kgf to detect possible variations of the hardness through the sections of the cuboids. Different colors are used to represent the three lines along which the indentations are taken (blue, black, and red). Along each line, the indentations are placed sufficiently apart from each other to avoid the results being affected by the local deformations of the neighbor indentations. As shown in the adjacent plots (Figure 3h,i), the average hardness is 165 HV0.2 for the flat cuboid and 155 HV0.2 for the vertical cuboid. The color scheme used in this figure helps us understand that there is no demarked hardness trend related to the location of the indentation. Nevertheless, it is important to mention that indentations taken in proximity to voids or pores gave a lower value of the hardness. To avoid the indenter from interacting with the voids, extra care was used to place the lines of indentations in between the bands of pores in the case of the vertical cuboid. Nonetheless, due to the high density of pores, it is possible that some indentations were too close to the voids. This is possibly the reason why the vertical cuboid is characterized by a slightly reduced hardness in comparison to the horizontal one, and the data points are more dispersed along the mean line, depicted with a dashed black line in the plots in Figure 3h,i.

### 3.2 | Three-Point Bending Tests

3PB tests were carried out with a rate of 1 mm/min in a 20-kN load cell machine with the fixture depicted in Figure 2. The span between the lower supports was 24 mm and the diameters of the rollers were 6 mm (upper one) and 3 mm (lower ones). As previously mentioned, the tests were programmed to stop at target displacement, which was considered safe to prevent damage to the fixture. None of the specimens reached complete failure, separating into two halves. For further analysis, the fracture surfaces of some selected specimens were separated in bending after the automatic arrest of the tests. For each cuboid, nine specimens were tested, three per notch radius. The load–vs.–load line displacement (LLD) curves obtained are shown in Figure 4a, but for the sake of clarity, the two orientations are separated in Figure 4b,c, and the curves are also grouped based on the notch radius in Figure 4d,f. Three relevant observations can be pointed out regarding these plots, which will be further confirmed by other analyses:

i. *Effect of the building orientation*: The specimens extracted from the horizontal cuboid are characterized by larger peak load and displacement at peak load. The average peak loads registered for the sharpest notch tested, 0.25 mm, are respectively 1300 and 1008 N for horizontal and vertical specimens, 1491 and 1078 N for the 0.5-mm notch radius, and 1627 and 1194 N for the largest notch ($\rho = 1$ mm). The percentage reduction of the peak loads from horizontal to vertical specimens is on average 26%, specifically 27% and 28% for the bigger notch radii of 0.5 and 1 mm, while 22% for the sharper notch of 0.25 mm. These data highlight that the difference among the building orientations becomes less relevant with increasing sharpness of the notch.

ii. *Effect of the notch radius*: Basic 2D numerical models were analyzed in the FE software Abaqus to calculate the stress concentration factor $k_t$, obtained as the ratio of the maximum stress in a notched specimen over the maximum stress in an unnotched specimen with the same width, subjected to the same boundary conditions. The values obtained are respectively 4.3, 5.6, and 7.4 for the notch radii of 1, 0.5, and 0.25 mm. These values suggest the magnitude of the notch sharpness effect in the intensification of the stress field in the specimens. This is confirmed by the results of the tests, which for the sake of clarity are also represented in Figure 4g. For both orientations, the peak loads decrease with decreasing notch radius, with the sharpest decrease in the case of the horizontal specimens.

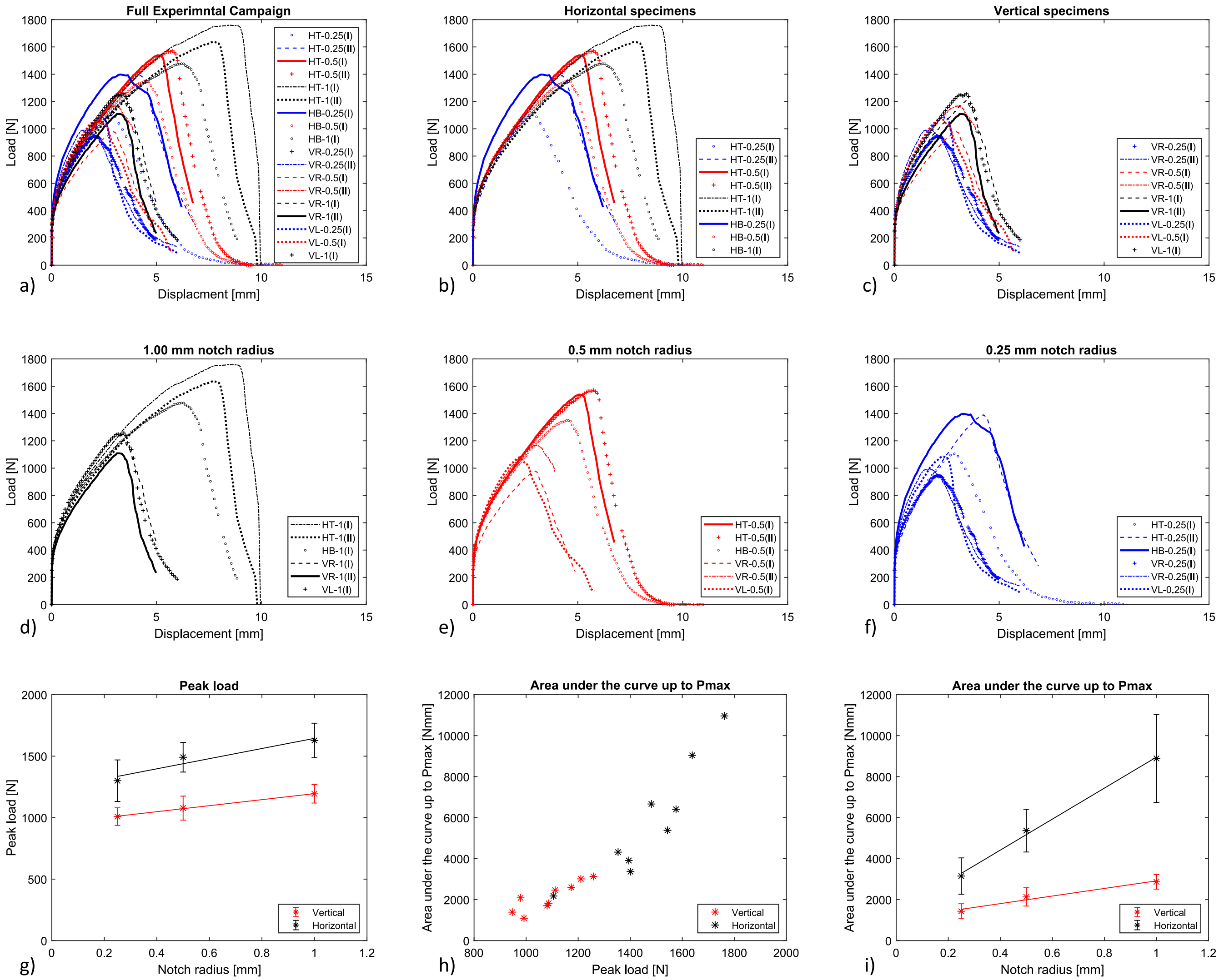


**FIGURE 4** | In the first row, the plots representing the complete experimental campaign (a), the horizontal specimens (b), and the vertical specimens (c) are shown. In the second row, the plots (d–f) are divided per notch radius. The following colors are assigned for the sake of clarity: black for $\rho = 1$ mm, red for $\rho = 0.5$ mm, and blue for $\rho = 0.25$ mm. In the third row, (g) peak load vs. notch radius trends; (h) integral of the load–LLD curves up to the peak load of each specimen, plotted vs. the peak loads and vs. the notch radius (i). [Colour figure can be viewed at wileyonlinelibrary.com]

iii. *Combined effect of notch radius and building orientation*: The building orientation significantly affects not only the numerical results of the tests but also the scatter among data. The specimens extracted from the vertical cuboid do not seem to be significantly affected by the notch radius, and the load–displacement curves of all specimens fall in the same range. This can be inferred by Figure 4c, but also by Figure 4h,i. In those plots, the area under the load-vs.-LLD curve is calculated up to the peak load for every specimen. In Figure 4h the area is plotted vs. peak load, revealing that all the vertical specimens populate the bottom left corner of the plot, while the horizontal specimens are more dispersed. The different impact of the notches in the two orientations is also visible in Figure 4i, where the area under the curves is plotted vs. the notch radius. The linear trend line drawn for the horizontal specimens has a slope significantly higher in comparison to that of the vertical specimens. The trend also suggests a possible intersection of the trend lines for smaller notch radii.

## 3.3 | Notch Deformation Mechanisms

The peak load of three-point bending tests is far from the final point of fracture. The tested specimens deform conspicuously after the peak, and the load does not drop abruptly from the maximum point, entailing that the fracture energy is high. For a better understanding of the sequence of notch deformation phases during the tests, Figure 5 represents the deformed specimens at known displacement values during the test. Six specimens were chosen to represent the three notch radii for both orientations. The figure is divided into sections, and the first three, Sections A, B, and C, are dedicated respectively to specimens with notch radii of 1, 0.5, and 0.25 mm. While the tests were performed, pictures were collected to be able to calculate the notch mouth opening displacement (NMOD) through DIC, which is also plotted vs. displacement. Note that the reported NMOD is obtained by measuring the opening of the notch from the bottom side of the specimen, excluding the opening of the undeformed notch, which corresponds to $2\rho$ since, in this notch geometry, the flanks of the notch are parallel.

### 3.3.1 | Effect of the Notch Radius on the Notch Deformation

The use of the DIC requires painting the specimens with a black-and-white speckle pattern that reduces the visibility of the fracture area. Nonetheless, the selected pictures reported on the right side of Figure 5 allow us to distinguish two main phases of deformation, common to every notch size and orientation. During the first phase, the notch opening is stable. No cracks or significant signs indicating the approach of the peak load are visible, and therefore, it is not possible to recognize from the pictures when the specimen is about to fail. The curvature of the notch tip increases until the tip becomes a flat edge. At a certain point, short cracks appear at the center of the notch, which propagates until the end of the tests. The moment in which the cracks appear represents the transition into the second phase of the deformation process. From the DIC pictures, it is difficult to identify the point of the first appearance of the crack. Intuitively, the transition from Phases 1 to 2 should correspond to the peak load, but a careful observation of the DIC images proved the contrary. It is possible to speculate that this point corresponds to the moment in which the NMOD-vs-LLD curves present an abrupt change of slope. The plots show that the displacement corresponding to the peak load increases with increased notch radius. The material shows a hardening behavior, characterized by increased stress as a response to increased deformation, which is not affected in a significant way by the notch radius, as shown in Figure 4. Therefore, higher displacements correspond to higher peak load as well. As much as the peak load moves towards the upper right corner of the plots, the transition point in the NMOD–LLD curves also moves to the right, which means that higher displacement is required to allow the initiation of a crack from notches with increased notch radius. In other words, the bluntest notches can allocate more plastic deformation than their counterparts. To investigate the point at which allegedly the cracks open, some extra pictures are reported for the specimen HT-1(II), attached in Figure 5 (Section D). The three details represent the displacement corresponding to the peak load, the displacement corresponding to the change in the trend of the NMOD, and one of the last points, in which it was possible to clearly distinguish the crack that appeared. To confirm the previous observation, the magnification *I*, corresponding to the peak load, does not offer any sign of imminent fracture. Interestingly, detail *II* also does not show anything different from detail *I*. Only after several pictures is it finally possible to individuate signs of a crack. It must be noted that the DIC may not be the most suitable method to deal with large plastic deformation, as in the present case [58]. As explained earlier, the focus of the work was merely to capture macroscopical distances as the opening of the notch mouth, for which the DIC is still reliable. Nonetheless, it is not possible to ensure the continuity between the paint and the specimens. It might be that the paint detached slightly from the underneath metal, concealing the initiation of the crack that becomes visible only after a certain amount of deformation, enough to crack the layer of paint.

### 3.3.2 | Effect of Building Orientation on Notch Deformation

As observed from the plots in Figure 4, the building orientation strongly affects the peak loads, the fracture energy absorbed by the specimens, and the notch radius effect. For one side, the peak load reduction registered for the vertical specimens is due to the unfavorable orientation of the layers with respect to the loading direction, which is an effect widely investigated in the case of tensile tests. On the other side, it was noticed from the results reported in the previous sections that the building orientation does not affect the microstructure and texture of the specimens, but it strongly affects the quantity and distribution of the printing-induced porosity, earlier described. It can be inferred that the porosity affects the performance of the specimens.

Figure 6 is dedicated to the comparison of a horizontal specimen and a vertical specimen with a notch radius of 1 mm, observed after the test. The pictures presented were taken with

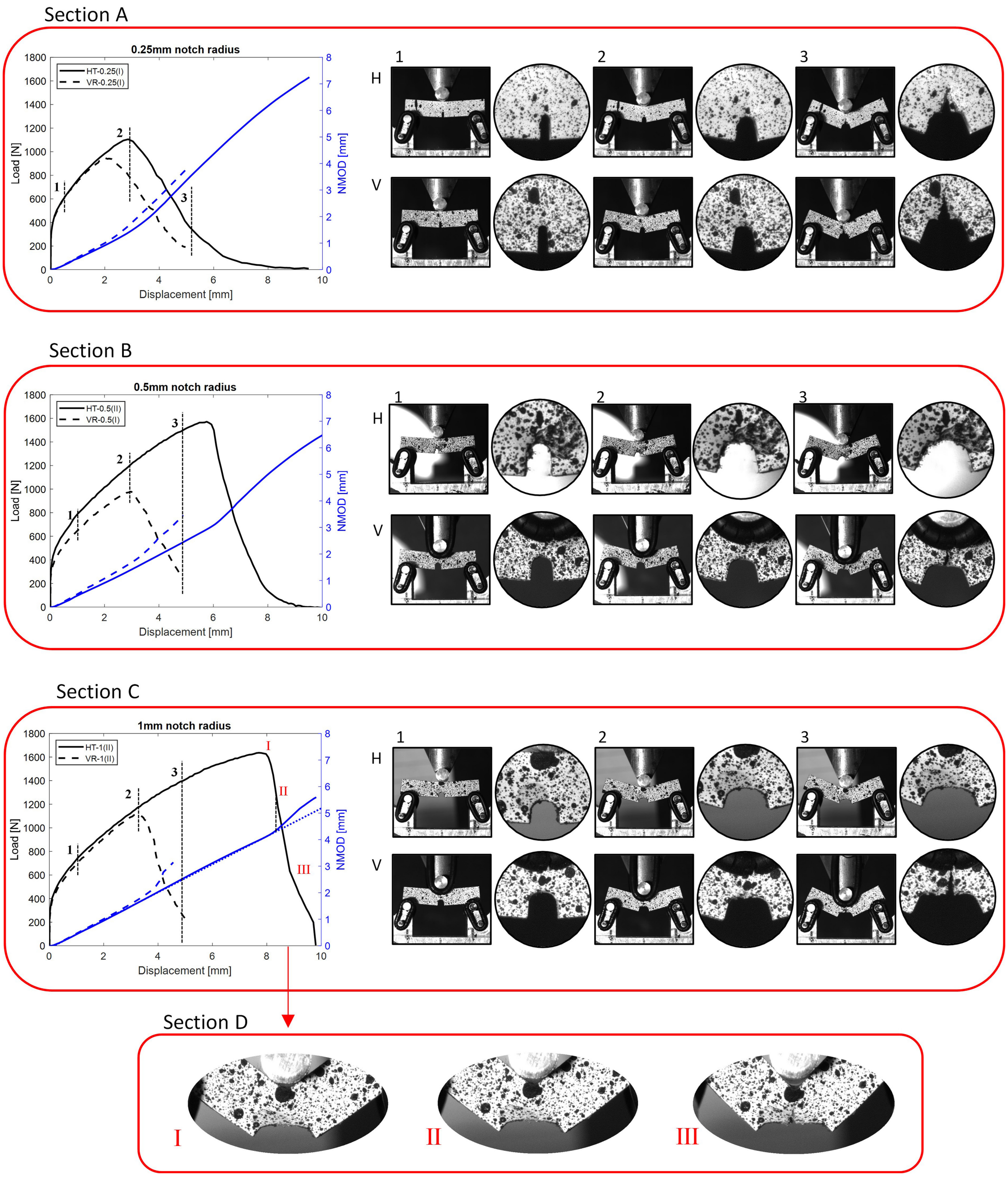


**FIGURE 5** | Sections A, B, and C report for each notch size a comparison plot of the load and NMOD vs. displacement for both building orientations. The adjacent pictures collect details of various moments of the tests numbered from 1 to 3. Section D reports three different magnifications of specimen HT-1(II) in an attempt to capture the crack initiation. [Colour figure can be viewed at wileyonlinelibrary.com]

both the SEM and the IFM confocal microscopes. The paint used for the DIC was removed to allow an easier observation of the interaction of the cracks with the voids. As confirmed from the fractography study in the next sections, it is assumed that the mechanism of the ductile fracture occurring in both orientations is related to void coalescence. In the case of the vertical specimen (Figure 6a, the crack path shows a zigzag pattern, jumping from one array of voids to the following. The intensity of the stress field in the area around the notch tip provoked deformation of the voids, potentially causing the necking of the material between them and gradually reducing the distance between adjacent voids, which eventually merged. This effect is less visible in the horizontal specimens (Figure 6b) due to the higher degree of densification of the material. Nonetheless, the magnification of the crack tip in the horizontal specimen shows a touch of alternating orientation of the crack tip as well. The pictures taken with the confocal microscope increase the visibility of the extended process zone around the deformed notch, which is not visible from the SEM pictures. This area is characterized by high plastic deformation, resulting in increased roughness, which resembles a darker color under optical light (Figure 6a1,b1). The pictures are also processed to show the height of the points through colors, considering as reference plane the opening of the notch

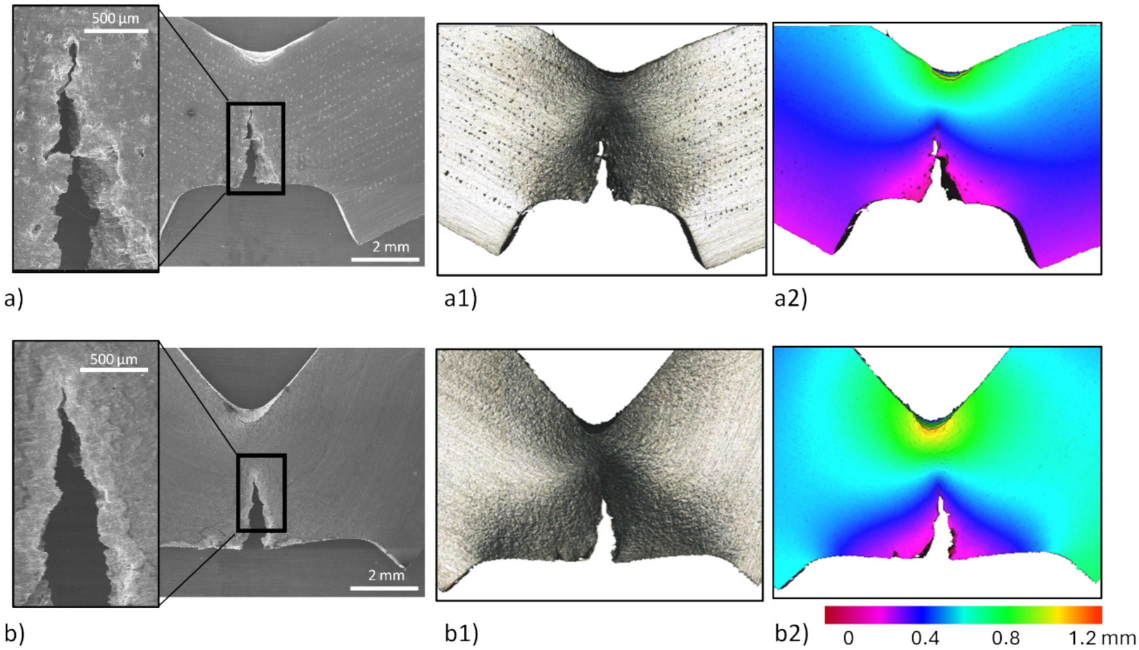


**FIGURE 6** | Magnification of the cracks originating from the deformed notch tip of the specimens VR-1(II) in the top row and HT-1(II)in the bottom row. (a, b) SEM pictures; (a1, b1) confocal microscope pictures; (a2, b2) representation of the out-of-plane deformation obtained from the confocal microscope surface characterization. [Colour figure can be viewed at wileyonlinelibrary.com]

on the edge of the specimens (Figure 6a2,b2). The colors highlight how transversally deformed are the specimens. In general, for a relatively similar crack length, the higher fracture resistance of the horizontal specimens, thanks to their higher density, has resulted in a considerably larger damage zone around the notch.

## 3.4 | Fracture Surface Analysis

Figure 7 collects some fracture surface pictures taken with the SEM and IFM confocal microscopes. In the top row (Row I), a representative fracture surface for each notch size for both printing orientations is shown. Schematics of the specimens are drawn on top of every picture to help understand from which cuboid the specimens were extracted and what is the relation between building orientation and loading direction. The second row (Row II) shows the morphological features of the fracture surfaces. The color scheme is meant to represent the height and the depth of the surfaces' features, considering as reference plane the symmetry plane of the notch in undeformed conditions.

### 3.4.1 | Fracture Mechanisms

In both types of fracture surface representation (SEM pictures and morphological images), there are no evident differences between notch sizes, while the building orientation is immediately perceivable. The inclined rectilinear rasters in the vertical specimens are obvious: both directions, 45°/−45°, are discernible, hinting that the fracture did not propagate on a single plane. The horizontal specimens appear more homogeneous, although the first specimen, HT-0.25(I), shows a surface pattern as well. The pattern suggests a horizontal alignment of pores that will be investigated with higher magnification pictures. Another remarkable difference between the two orientations is the enhanced lateral deformation that the horizontal specimens show in comparison to their vertical counterparts, which is in line with the confocal microscopy results in Figure 6 and attributed to the greater required energy for fracture. In the horizontal specimens, the free surfaces of the notches are more significantly deformed, and signs of surface cracking can be observed for the larger notches where the notch deformation during the test was higher, leading to excessive opening of the notch and potentially facilitating the appearance of small cracks from the surface of the notch. In general, both orientations display a ductile fracture, characterized by very rough surfaces and instability of the crack plane, as suggested by the change in the colors of the figures in Row II. In the very first section of this paper, it was highlighted that the perpendicularity of the load direction with the building direction (which in the present work is the case of the vertical specimens) is likely to provoke delamination of the layers. Some examples of this kind of fracture can be seen in [24, 59], where the surfaces are mainly flat and do not present any typical ductile features such as dimples. On the contrary, the vertical fracture surfaces depicted here are rough, and there are no signs of cleavage or delamination. Therefore, it is possible to conclude that also the vertical specimens experienced ductile fracture since the layer's interfaces were successfully bonded.

### 3.4.2 | Building Orientation Effect and Printing-Induced Porosity

Row III is focused on the investigation of the fracture features visible on the first specimen, HT-0.25(I). The surface is covered with dimples and appears decently dense. Nonetheless, there is an

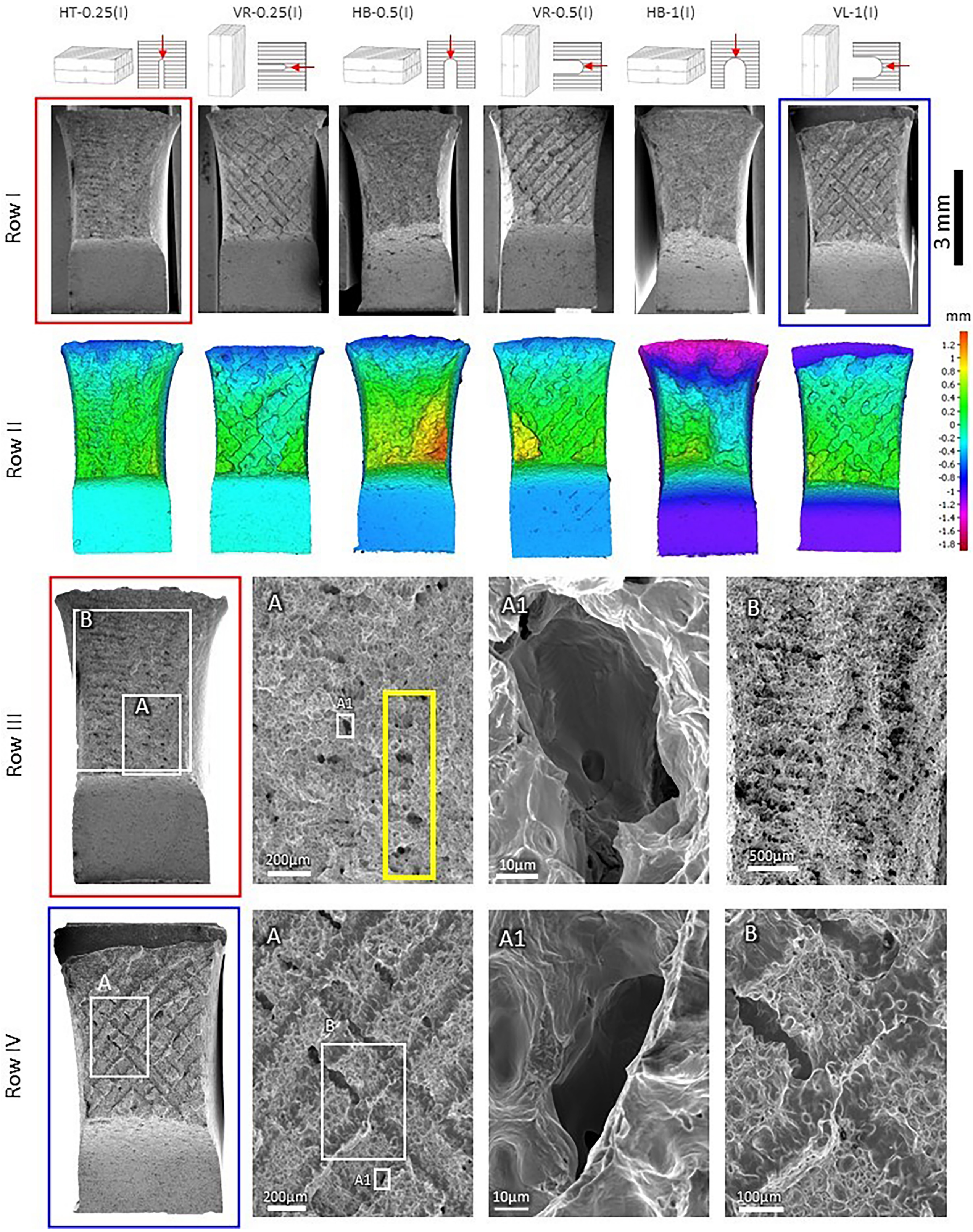


**FIGURE 7** | (Row I) SEM pictures of six representative specimens for every notch radius in both building orientations. The schematics above the pictures shall help us understand the loading direction and the building orientation; (Row II) morphological pictures of the same specimens; (Row III) fractographical study on specimen HT-0.25(I), highlighted in red in the first row; (Row IV) fractographical study on specimen VL-1(I), highlighted in blue in the first row. [Colour figure can be viewed at wileyonlinelibrary.com]

abundance of deep voids like the one depicted in Detail A1. The surfaces inside the void are smooth, with signs of microstructural deformation on the grains and the grain boundaries. Such defects possibly originated from the inherent microstructure of MEAM process or "kissing bonds," which are areas in which the deposited rasters were touching each other without sufficient compenetration to guarantee material continuity after debinding and sintering [60]. During the bending tests, those defects deformed with the rest of the material, becoming larger. At first sight, these voids appear randomly distributed, but in some areas of the fracture surfaces, they create a specific pattern: For example, in Magnification A, a vertical alignment of pores is highlighted with a yellow contour. This suggests that these voids have the same origin described earlier for the vertical specimens, as depicted in the schematic in Figure 3e. On the left side of the specimens, another pattern can be observed and magnified in Detail B, which consists of some horizontal ridges of material. This horizontal alignment suggests a possible correspondence with the layers, meaning that the layer interfaces are not perfectly continuous. Similar features were observed in [61]. Interestingly, this is the only horizontal specimen in which this feature is visible.

Row IV shows the vertical specimen VL-1(I) with a 1-mm notch radius. The alternating rectilinear pattern is completely exposed, and in some areas of the fracture, a checkered pattern appears (Detail A). Higher magnifications (Detail B) revealed that the infill of the "checks" is disseminated with dimples, while the borders of the checks are smoother and darker, therefore deeper. This feature is related to what was observed on the surfaces of the vertical specimens described in some previous paragraphs and depicted in Figure 3e. While from that picture it was not possible to guess the depth of the voids, from these SEM pictures, we can understand that the almost spherical voids were cross sections of long empty channels that run all along the rasters. The walls of these channels are the darker longilineal lines visible in the SEM pictures that present smoother walls, although crazes of sintered powders on the free surfaces are visible. The same effect can be observed in Figure 1, in the magnification related to the postsintering material appearance. They do not present either ductile or fragile fracture features. Only some bumps are related to the diffusion of the material and the growth of the grains during sintering. Considering the ratio of the surface invested by ductile fracture (the infill of the checks) and the portion of voids along the rasters, it is possible to conclude that the volume of material in front of the notch is considerably smaller for vertical specimens than for horizontal specimens. Moreover, it seems that the channels are connected from layer to layer although it is not possible to say if the connection occurred while the material was deforming. This is suggested by the increased darkness of some portions of the channels (Detail A). Some deep elongated voids (Detail A1) are also visible on the surface, corroborating the thesis of the interconnected channels. Connected porosity channels were also observed by Damon et al. [13] as a specific feature of the specimens printed with alternating raster angles.

### 3.5 | Numerical Investigation

In the present section, the application of the ASED and TCD criteria is presented. The calibration required for both methods is described in Appendix I. The size of the dataset available is unfortunately limited to achieve a reliable calibration. Nonetheless, the scope of the work is restricted to the evaluation of the potentialities of the abovementioned methods to predict the failure of notched 316L MEAM specimens with the available test data.

In the first place, it is required to model the specimens in FE software with a linear elastic material model. The tensile properties of horizontal and vertical specimens, reported in Figure 8 (Table I), are significantly different. The difference in terms of tensile strength can be quickly reduced to the unfavorable parallelism of building direction and loading direction [14, 16]. On the contrary, it is interesting to notice the significant discrepancy among Young's modulus $E$ reported in Figure 8 (Table I) (153 and 125 GPa for horizontal and vertical specimens, respectively), and the average value of Young's modulus of stainless steel (close to 200 GPa [48]). The reduction is probably due to the porosity of the material since the relative density affects the elasticity of the metals [63, 64]. The investigation on the porosity content reported previously confirms this deduction. Moreover, since it was observed that vertical cuboids are affected by more extensive printing-induced porosity, the difference between horizontal and vertical $E$ is also explained.

From a microstructural and microhardness perspective, horizontal and vertical cuboids did not show any significant differences. Therefore, the anisotropy observed in both Figure 8 (Table I), which presents the tensile properties of the material for each building orientation, and Figure 4, which shows the results of the 3PB tests, cannot be attributed to microstructural features. The primary cause of this anisotropy is related to the orientation of the loading direction relative to the building direction. As fully disclosed in [12, 15], stresses parallel to the layers are better sustained than stresses acting perpendicularly. This effect is likely exacerbated by the residual porosity observed in the samples. Consequently, it can be argued that microhardness may not be a suitable indicator of the mechanical properties of a material with such significant anisotropy, whose origin is primarily macroscopical.

The average tensile properties were calculated to apply the criterion. As described in Appendix I, the ASED criterion requires as input the tensile properties and the fracture toughness $K_{Ic}$ of the material, which must be defined. According to the ASTM standard E1820, the fracture toughness can be obtained using a SEN-B specimen where a sharp crack starting from the notch tip is obtained with a procedure of fatigue precracking. Since this step was not performed before the 3PB tests, only an approximate value of the toughness, $K^*_{Ic}$ can be obtained, using the formulations available in the standard with the peak load recorded during the tests. It was chosen to use only the data relative to the sharpest notches, $\rho = 0.25$ mm, since the stress field in these specimens is the most intensified, the closest available to the singularity that a physical crack would determine. A similar procedure was followed in [65], where an "apparent" value of $K_{Ic}$ is found with notched specimens that were not precracked. The authors explained that the blunter the notch, the larger the plastic deformation area around it, leading to more conservative values of the fracture toughness. Moreover, in [66], a comparison between precracked and notched tension specimens revealed that for fracture toughness calculations based on the peak load, the precracking procedure was not fundamental. In

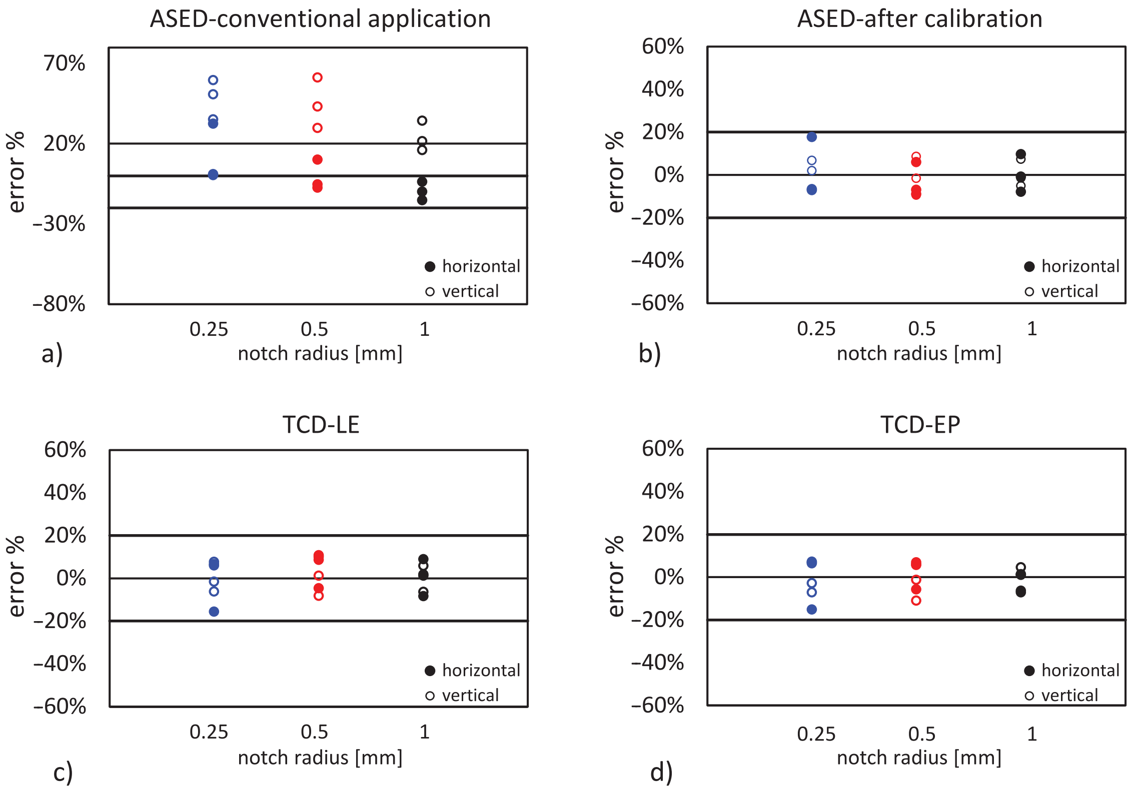


| Table I | $\sigma_{UTS}$ MPa | $E$ GPa | $v$ | $K^*_{Ic}$ MPa√m |
|---|---|---|---|---|
| H | 509 | 153 | 0.35 | 38.8 |
| V | 437 | 125 | 0.35 | 30.1 |

| Table II | $R_c$ mm | $\sigma_t^*$ MPa | $K_{Ic}$ MPa√m | $L_{c\text{-}LE}$ mm | $\sigma_0$ MPa | $K_{Ic}$ MPa√m | $L_{c\text{-}EP}$ mm | $\sigma_0$ MPa | $K_{Ic}$ MPa√m |
|---|---|---|---|---|---|---|---|---|---|
| H | 0.13 | 1727 | 39.7 | 0.19 | 1712 | 41.3 | 0.39 | 913 | 31.9 |
| V | 0.15 | 1356 | 34.5 | 0.22 | 1207 | 32 | 0.66 | 672 | 30.6 |
| | ASED-calibration | | | TCD-Linear elastic models | | | TCD-Elasto-plastic models | | |

**FIGURE 8** | (a, b) Graphical representations of the accuracy of the ASED prediction before and after calibrations; (c, d) TCD accuracy using linear elastic models (LE) and elastoplastic models (EP). Table I contains the tensile properties obtained for horizontal and vertical specimens, and the results of the apparent fracture toughness $K^*_{Ic}$ [62]. Table II summarizes the results of the methods used, the ASED criterion after calibration, and the TCD with LE and EP models. [Colour figure can be viewed at wileyonlinelibrary.com]

light of these works, the so-called apparent fracture toughness ($K^*_{Ic}$), as we decided to call it, was here obtained, separately for vertical and horizontal specimens. The values are reported in Table I of Figure 8, and an average was used to calculate $R_c$. With this set of inputs, the failure loads are calculated ($P_{FEM}$) and compared with the peak loads obtained experimentally ($P_{exp}$) (Figure 8a), revealing that the method is not capable of precise predictions. The relative error used to compare the results is calculated as $(P_{FEM} - P_{exp})/P_{exp}$. To improve the accuracy of the ASED criterion, it was considered necessary to separate the two building orientations since the differences in the tensile behavior of vertical and horizontal specimens are not negligible, and average properties would not be representative of either of the cases. This action was proven to be insufficient, leading to the second realization that the values hypothesized for $W_c$ and fracture toughness (and consequently $R_c$) were inadequate. A calibration procedure, described in Appendix I, was carried out to individuate the correct inputs. The calibration was successful, as depicted in Figure 8b, and the new predicted values of the failure load appear to be contained in a scatter band of ±20%, which is considered a reasonable scatter [33]. The increased accuracy is obtained by reducing significantly the size of the control volume. The $R_c$ calculated as a first attempt was 1.25 mm, which is a considerable size compared to the specimens' dimensions. After the calibration, the $R_c$ is reduced to 0.13 and 0.15 mm, respectively, for horizontal and vertical specimens. These values are surprisingly similar, although, in the first place, it was considered paramount to separate the building orientations.

The PM of the TCD was also calibrated to find the characteristic material length parameter $L_c$ through a procedure also described in Appendix I. The length parameter is then used to individuate the inherent material strength $\sigma_0$ acting as the upper limit of the stress to avoid failure. The values obtained are coherent with the results of the ASED criterion: The material lengths (named $L_{cLE}$ as a reminder that the material models used were linear elastic) are, for example, 0.19 and 0.22 mm, respectively, for horizontal and vertical specimens. Once again, the two groups of specimens are characterized by very similar results. The values of the inherent material strength are 1712 and 1207 MPa, which are unrealistic values, exceedingly more than three times the UTS of the material. The reason behind this result is that the plasticity of the material is not taken into account at all. Besides this inconsistency, in the work by Susmel and Taylor [28] in which the TCD was successfully used to predict the static failure of notched ductile specimens using linear elastic models, it was stated that the inherent material strength does not necessarily have a physical meaning.

To prove the validity of this assumption, other analyses with an elastoplastic material model were implemented. The material models were obtained tabularly using the data from the tensile tests and considering vertical and horizontal specimens as two different cases. A plane strain field was considered. The calibration of the TCD with elastoplastic models was more time-consuming. Nonetheless, the stress fields were analyzed to determine new material length scale parameters. The values obtained are 0.39 and 0.66 mm, respectively, for horizontal and vertical specimens, which are greater than the ones obtained with LE models. The predictions of failure conditions obtained when implementing the elastoplastic characteristic length ($L_{cEP}$) were proven to be a more precise LE prediction, but not in a significant way, as depicted in Figure 8c,d, where the error is obtained as $(\sigma_{eff}-\sigma_0)/\sigma_0$. In conclusion, it is possible to assume that the linear elastic models can be used successfully to determine the characteristic length of a very ductile material such as the MEAM 316L stainless steel at room temperature.

From both the ASED and TCD procedures, it is possible to calculate backward the fracture toughness that should have been the input of the two methods to assure perfect calibration. Moreover, it is possible to calculate the value that should have been used as $\sigma_t$ in the conventional application of ASED. These values are listed in Figure 8 (Table II). Since they exceed the material strength and they do not have the physical meaning of the UTS of the material, they are denominated, $\sigma_t^*$. These apparent tensile strengths are in good accordance with the inherent material strength $\sigma_0$ calculated in the application of TCD with linear elastic models. The inherent material strength obtained in the case of elastoplastic models is significantly reduced but still not comparable to the tensile strength of the material. A possible reason is related to the degree of precision of the FE models implemented, which were not designed to simulate the behavior of the components with accuracy but were instead used to assess the consistency of the linear elastic models. The different values of fracture toughness obtained according to the different methods used are quite aligned with each other.

## 4 | Conclusion and Recommendations

The notch effect on the bending behavior of 316L SS specimens fabricated via MEAM has been investigated considering three different notch sizes. The study also proposed to investigate the building direction effect on the tests performed, and some important conclusions can be drawn:

1. The horizontal and vertical cuboids are characterized before cutting them to extract the specimens. The building orientation is proven to not affect the microstructure, which appears to be the typical microstructure of sintered stainless steel, with isotropic texture and relatively coarse grain size (average grain equivalent diameter of 44 μm). The effect on the microhardness is also mild, with average values of 165 and 155 HV0.2 for horizontal and vertical samples.
2. Conversely, the porosity distribution is highly dependent on the building direction. The reason is probably related to the challenges that the print of a relatively thin and relatively tall body, such as the vertical cuboid, entails. As a result, in the vertical specimens, the presence of interconnected channels of pores reduced drastically the density of the material, with consequences on the mechanical properties as well. The horizontal specimens were denser and more homogeneous, suggesting a successful manufacturing process. Nonetheless, the fractography study reported in the previous section highlighted several discontinuities and voids in the horizontal specimens as well.
3. The notch radius strongly affected the bending response, provoking a decrease in the peak load as the notch size decreases. This is a result of the milder stress intensification induced by the bluntest notch investigated, $\rho = 1$ mm.
4. The building orientation was indeed the most significant factor in the determination of the bending performances. The horizontal specimens, independently of the notch radius, are characterized by higher peak load, longer displacement, and higher energy to fracture. The observation of the notch deformation showed that the notches cut from horizontal specimens are capable of larger deformation, completely transforming the shape of the original notch. This is due to a combination of effects: (i) the more favorable orientation of building direction and loading direction and (ii) the higher density of the horizontal specimens.
5. The vertical specimens proved to be less affected by the notch size since a 15% difference was observed in the bending tests peak loads obtained with the 1- and 0.25-mm notch sizes. On the contrary, in the horizontal specimens, the impact of the sharpness of the notches was more demarked, around 20%. This is possibly also a result of the

printing-induced porosity, creating a predamage whose effect is not altered by the severity of the notches.

6. The numerical tools ASED and TCD were successfully calibrated to represent the failure conditions of the specimens although the material does not meet the requirements and limitations of the tools. Moreover, it was proven to be beneficial to consider the two building orientations as different materials due to the great scatter between the results of the mechanical tests.

The impact of the build orientation on the bending behavior of notched specimens revealed in the present study is a paramount issue to consider during the design of a component. It is already well-known that the orientation of an additively manufactured part affects the feasibility of features like overhangs and notches, to reduce the need for support material. Hence, whenever the feasibility requirements do not meet the resistance requirements here illustrated, a redesign of the part must be considered. Further experimental campaigns must be planned to uncouple the effect of the anisotropy related to the layer orientation and the porosity distribution that has been proven to be also dependent on the building orientation. Different strategies must be implemented to increase the predictability of the porosity distribution in the parts. Lastly, it must be highlighted that the notches studied in the present work were machined. In the case of printed notches, different factors would come into play, such as the effect of the outer contours. The present study is therefore a useful starting point for more specific investigations on the limitations of parts and components produced with MEAM.

## Nomenclature

| | |
|---|---|
| 3PB | three-point bending tests |
| AM | additive manufacturing |
| ASED | average strain energy density |
| DIC | digital image correlation |
| EDM | electric discharge machine |
| EP | elastic–plastic |
| LE | linear elastic |
| LEFM | linear elastic fracture mechanics |
| LLD | load line displacement |
| MEAM | material extrusion additive manufacturing |
| NMOD | notch mouth opening displacement |
| PM | point method |
| TCD | theory of critical distance |
| UTS | ultimate tensile strength (ductile materials) |
| $K_{Ic}$ | fracture toughness |
| $K^*_{Ic}$ | apparent fracture toughness |
| $k_t$ | stress concentration factor |
| $L_c$ | critical length parameter |
| $P_{exp}$ | experimental peak load |
| $P_f$ | failure load |
| $P_{FEM}$ | numerically predicted failure load |
| $\rho$ | notch radius |
| $R_c$ | control volume radius |
| $\sigma_0$ | inherent material strength |
| $\sigma_{eff}$ | effective stress |
| $\sigma_t$ | tensile strength (brittle materials) |
| $\sigma^*_t$ | apparent tensile strength |
| $\overline{W}$ | average strain energy density |
| $W_c$ | critical strain energy density |

## Author Contributions

**Saveria Spiller:** conceptualization, methodology, formal analysis, validation, investigation, writing – original draft, visualization, data curation. **Sara Couto:** formal analysis, investigation. **Nima Razavi**: conceptualization, methodology, investigation, writing – review and editing, supervision, resources.

## Data Availability Statement

The data that support the findings of this study are available from the corresponding author upon reasonable request.

## References

1. G. Prashar, H. Vasudev, and D. Bhuddhi, "Additive Manufacturing: Expanding 3D Printing Horizon in Industry 4.0," *International Journal on Interactive Design and Manufacturing* 17 (2022): 2221–2235, https://doi.org/10.1007/s12008-022-00956-4

2. M. Attaran, "The Rise of 3-D Printing: The Advantages of Additive Manufacturing Over Traditional Manufacturing," *Business Horizons* 60 (2017): 677–688, https://doi.org/10.1016/j.bushor.2017.05.011

3. S. Ford and M. Despeisse, "Additive Manufacturing and Sustainability: An Exploratory Study of the Advantages and Challenges," *Journal of Cleaner Production* 137 (2016): 1573–1587, https://doi.org/10.1016/j.jclepro.2016.04.150

4. A. Vafadar, F. Guzzomi, A. Rassau, and K. Hayward, "Advances in Metal Additive Manufacturing: A Review of Common Processes, Industrial Applications, and Current Challenges," *Applied Sciences* 11, no. 3 (2021): 1213, https://doi.org/10.3390/app11031213

5. Additive Manufacturing—General Principles—Terminology, ISO/ASTM 52900, 2015.

6. S. Wickramasinghe, T. Do, and P. Tran, "FDM-Based 3D Printing of Polymer and Associated Composite: A Review on Mechanical Properties," *Polymers (Basel)* 12, no. 7 (2020): 1529, https://doi.org/10.3390/polym12071529

7. colorFabb, 2024, https://colorfabb.com/

8. the Virtual Foundry, 2024, https://thevirtualfoundry.com/

9. J. Gonzalez-Gutierrez, S. Cano, S. Schuschnigg, C. Kukla, J. Sapkota, and C. Holzer, "Additive Manufacturing of Metallic and Ceramic Components by the Material Extrusion of Highly-Filled Polymers: A Review and Future Perspectives," *Materials (Basel)* 11 (2018): 840, https://doi.org/10.3390/ma11050840

10. M. Armstrong, H. Mehrabi, and N. Naveed, "An Overview of Modern Metal Additive Manufacturing Technology," *Journal of Manufacturing Processes* 84 (2022): 1001–1029, https://doi.org/10.1016/j.jmapro.2022.10.060

11. S. Spiller, S. Olsøybakk Kolstad, and N. Razavi, "Fatigue Behavior of 316L Stainless Steel Fabricated via Material Extrusion Additive Manufacturing," *Engineering Fracture Mechanics* 291 (2023): 109544, https://doi.org/10.1016/j.engfracmech.2023.109544

12. M. Á. Caminero, A. Romero, J. M. Chacón, P. J. Núñez, E. García-Plaza, and G. P. Rodríguez, "Additive Manufacturing of 316L Stainless-Steel Structures Using Fused Filament Fabrication Technology: Mechanical and Geometric Properties," *Rapid Prototyping Journal* 27 (2021): 583–591, https://doi.org/10.1108/RPJ-06-2020-0120

13. J. Damon, S. Dietrich, S. Gorantla, U. Popp, B. Okolo, and V. Schulze, "Process Porosity and Mechanical Performance of Fused Filament Fabricated 316L Stainless Steel," *Rapid Prototyping Journal* 25 (2019): 1319–1327, https://doi.org/10.1108/RPJ-01-2019-0002

14. T. Kurose, Y. Abe, M. V. A. Santos, et al., "Influence of the Layer Directions on the Properties of 316L Stainless Steel Parts Fabricated Through Fused Deposition of Metals," *Materials (Basel)* 13 (2020): 13, https://doi.org/10.3390/ma13112493

15. C. Suwanpreecha, P. Seensattayawong, V. Vadhanakovint, and A. Manonukul, "Influence of Specimen Layout on 17-4PH (AISI 630) Alloys Fabricated by Low-Cost Additive Manufacturing," *Metallurgical and Materials Transactions A, Physical Metallurgy and Materials Science* 52 (2021): 1999–2009, https://doi.org/10.1007/s11661-021-06211-x

16. T. Alkindi, M. Alyammahi, R. A. Susantyoko, and S. Atatreh, "The Effect of Varying Specimens' Printing Angles to the Bed Surface on the Tensile Strength of 3D-Printed 17-4PH Stainless-Steels via Metal FFF Additive Manufacturing," *MRS Communications* 11 (2021): 310–316, https://doi.org/10.1557/s43579-021-00040-0

17. Y. Abe, T. Kurose, M. V. A. Santos, et al., "Effect of Layer Directions on Internal Structures and Tensile Properties of 17-4ph Stainless Steel Parts Fabricated by Fused Deposition of Metals," *Materials (Basel)* 14 (2021): 1–12, https://doi.org/10.3390/ma14020243

18. W. Hassan, M. A. Farid, A. Tosi, K. Rane, and M. Strano, "The Effect of Printing Parameters on Sintered Properties of Extrusion-Based Additively Manufactured Stainless Steel 316L Parts," *International Journal of Advanced Manufacturing Technology* 114 (2021): 3057–3067, https://doi.org/10.1007/s00170-021-07047-w

19. T. C. Henry, M. A. Morales, D. P. Cole, C. M. Shumeyko, and J. C. Riddick, "Mechanical Behavior of 17-4 PH Stainless Steel Processed by Atomic Diffusion Additive Manufacturing," *International Journal of Advanced Manufacturing Technology* 114 (2021): 2103–2114, https://doi.org/10.1007/s00170-021-06785-1

20. A. Kasha, S. O. Obadimu, and K. I. Kourousis, "Flexural Characteristics of Material Extrusion Steel 316L: Influence of Manufacturing Parameters," *Additive Manufacturing Letters* 3 (2022): 100087, https://doi.org/10.1016/j.addlet.2022.100087

21. Y. Thompson, J. Gonzalez-Gutierrez, C. Kukla, and P. Felfer, "Fused Filament Fabrication, Debinding and Sintering as a Low Cost Additive Manufacturing Method of 316L Stainless Steel," *Additive Manufacturing* 30 (2019): 100861, https://doi.org/10.1016/j.addma.2019.100861

22. M. Carminati, M. Quarto, G. D'urso, C. Giardini, and G. Maccarini, "Mechanical Characterization of AISI 316L Samples Printed Using Material Extrusion," *Applied Sciences* 12, no. 3 (2022): 1433, https://doi.org/10.3390/app12031433

23. T. Rosnitschek, S. Tremmel, A. Seefeldt, B. Alber-Laukant, T. Neumeyer, and V. Altstädt, "Correlations of Geometry and Infill Degree of Extrusion Additively Manufactured 316L Stainless Steel Components," *Materials (Basel)* 14 (2021): 5173, https://doi.org/10.3390/ma14185173

24. S. Kedziora, T. Decker, E. Museyibov, et al., "Strength Properties of 316L and 17-4 PH Stainless Steel Produced With Additive Manufacturing," *Materials (Basel)* 15 (2022): 6278, https://doi.org/10.3390/ma15186278

25. N. Razavi, H. R. Majidi, F. Berto, and M. R. Ayatollahi, "Fracture Assessment of U-Notched Graphite Specimens by Means of Cohesive Zone Model," *Procedia Structural Integrity* 26 (2020): 251–255, https://doi.org/10.1016/j.prostr.2020.06.031

26. N. Razavi, H. Askes, F. Berto, and L. Susmel, "Length Scale Parameters to Estimate Fatigue Lifetime of 3D-Printed Titanium Alloy Ti6Al4V Containing Notches in the As-Manufactured Condition," *International Journal of Fatigue* 167 (2023): 107348, https://doi.org/10.1016/j.ijfatigue.2022.107348

27. H. Askes, P. Livieri, L. Susmel, D. Taylor, and R. Tovo, "Intrinsic Material Length, Theory of Critical Distances and Gradient Mechanics: Analogies and Differences in Processing Linear-Elastic Crack tip Stress Fields," *Fatigue and Fracture of Engineering Materials and Structures* 36 (2013): 39–55, https://doi.org/10.1111/j.1460-2695.2012.01687.x

28. L. Susmel and D. Taylor, "On the Use of the Theory of Critical Distances to Predict Static Failures in Ductile Metallic Materials Containing Different Geometrical Features," *Engineering Fracture Mechanics* 75 (2008): 4410–4421, https://doi.org/10.1016/j.engfracmech.2008.04.018

29. P. Seibert, D. Taylor, F. Berto, and N. Razavi, "Energy TCD—Robust and Simple Failure Prediction Unifying the TCD and ASED Criterion," *Engineering Fracture Mechanics* 271 (2022): 108652, https://doi.org/10.1016/j.engfracmech.2022.108652

30. F. Berto and P. Lazzarin, "Recent Developments in Brittle and Quasi-Brittle Failure Assessment of Engineering Materials by Means of Local Approaches," *Materials Science & Engineering R: Reports* 75 (2014): 1–48, https://doi.org/10.1016/j.mser.2013.11.001

31. S. Shahbaz, M. R. Ayatollahi, M. Petru, and A. R. Torabi, "U-Notch Fracture in Additively Manufactured ABS Specimens Under Symmetric Three-Point Bending," *Theoretical and Applied Fracture Mechanics* 119 (2022): 103318, https://doi.org/10.1016/j.tafmec.2022.103318

32. M. Sánchez, S. Cicero, S. Arrieta, and V. Martínez, "Fracture Load Predictions in Additively Manufactured ABS U-Notched Specimens Using Average Strain Energy Density Criteria," *Materials (Basel)* 15 (2022): 2372, https://doi.org/10.3390/ma15072372

33. P. Seibert, S. M. J. Razavi, L. Susmel, F. Berto, and M. Kästner, "Validation of the Averaged Strain Energy Density Criterion for Additively Manufactured Notched Polylactide Acid Specimens," *Procedia Structural Integrity* 28 (2020): 2099–2103, https://doi.org/10.1016/j.prostr.2020.11.035

34. C. T. Ng and L. Susmel, "Notch Static Strength of Additively Manufactured Acrylonitrile Butadiene Styrene (ABS)," *Additive Manufacturing* 34 (2020): 101212, https://doi.org/10.1016/j.addma.2020.101212

35. A. A. Ahmed and L. Susmel, "A Material Length Scale–Based Methodology to Assess Static Strength of Notched Additively Manufactured Polylactide (PLA)," *Fatigue and Fracture of Engineering Materials and Structures* 41 (2018): 2071–2098, https://doi.org/10.1111/ffe.12746

36. B. Gillham, A. Yankin, F. McNamara, C. Tomonto, D. Taylor, and R. Lupoi, "Application of the Theory of Critical Distances to Predict the Effect of Induced and Process Inherent Defects for SLM Ti-6Al-4V in High Cycle Fatigue," *CIRP Annals* 70 (2021): 171–174, https://doi.org/10.1016/j.cirp.2021.03.004

37. D. Taylor, M. Merlo, R. Pegley, and M. P. Cavatorta, "The Effect of Stress Concentrations on the Fracture Strength of Polymethylmethacrylate," *Materials Science and Engineering A* 382 (2004): 288–294, https://doi.org/10.1016/j.msea.2004.05.012

38. W. Li, L. Susmel, H. Askes, F. Liao, and T. Zhou, "Assessing the Integrity of Steel Structural Components With Stress Raisers Using the Theory of Critical Distances," *Engineering Failure Analysis* 70 (2016): 73–89, https://doi.org/10.1016/j.engfailanal.2016.07.007

39. L. Susmel and D. Taylor, "The Theory of Critical Distances to Estimate the Static Strength of Notched Samples of Al6082 Loaded in Combined Tension and Torsion. Part I: Material Cracking Behaviour," *Engineering Fracture Mechanics* 77 (2010): 452–469, https://doi.org/10.1016/j.engfracmech.2009.11.015

40. M. Rakin, Z. Cvijovic, V. Grabulov, S. Putic, and A. Sedmak, "Prediction of Ductile Fracture Initiation Using Micromechanical Analysis," *Engineering Fracture Mechanics* 71 (2004): 813–827, https://doi.org/10.1016/S0013-7944(03)00013-4

41. R. Muro-Barrios, Y. Cui, J. Lambros, and H. B. Chew, "Dual-Scale Porosity Effects on Crack Growth in Additively Manufactured Metals: 3D Ductile Fracture Models," *Journal of the Mechanics and Physics of Solids* 159 (2022): 104727, https://doi.org/10.1016/j.jmps.2021.104727

42. P. Lazzarin and R. Zambardi, "A Finite-Volume-Energy Based Approach to Predict the Static and Fatigue Behavior of Components With

Sharp V-Shaped Notches," *International Journal of Fracture* 112 (2001): 275–298, https://doi.org/10.1023/A:1013595930617

43. F. B. P. Lazzarin and F. J. G. M. Elices, "Fracture Assessment of U-Notches Under Mixed Mode Loading: Two Procedures Based on the 'Equivalent Local Mode I' Concept," *International Journal of Fracture* 148 (2008): 415–433, https://doi.org/10.1007/s10704-008-9213-7

44. D. Taylor, "The Theory of Critical Distances," *Engineering Fracture Mechanics* 75 (2008): 1696–1705, https://doi.org/10.1016/j.engfracmech.2007.04.007

45. S. Spiller, S. Olsøybakk, S. Mohammad, and J. Razavi, "Fabrication and Characterization of 316L Stainless Steel Components Printed With Material Extrusion Additive Manufacturing," *Procedia Structural Integrity* 42 (2022): 1239–1248, https://doi.org/10.1016/j.prostr.2022.12.158

46. S. Spiller, F. Berto, and S. M. Javad Razavi, "Mechanical Behavior of Material Extrusion Additive Manufactured Components: An Overview," *Procedia Structural Integrity* 41 (2022): 158–174, https://doi.org/10.1016/j.prostr.2022.05.018

47. P. Seibert, L. Susmel, F. Berto, M. Kästner, and N. Razavi, "Applicability of Strain Energy Density Criterion for Fracture Prediction of Notched PLA Specimens Produced via Fused Deposition Modeling," *Engineering Fracture Mechanics* 258 (2021): 108103, https://doi.org/10.1016/j.engfracmech.2021.108103

48. H. Gong, D. Snelling, K. Kardel, and A. Carrano, "Comparison of Stainless Steel 316L Parts Made by FDM- and SLM-Based Additive Manufacturing Processes," *JOM* 71 (2019): 880–885, https://doi.org/10.1007/s11837-018-3207-3

49. R. Santamaria, M. Salasi, S. Bakhtiari, G. Leadbeater, M. Iannuzzi, and M. Z. Quadir, "Microstructure and Mechanical Behaviour of 316L Stainless Steel Produced Using Sinter-Based Extrusion Additive Manufacturing," *Journal of Materials Science* 57 (2022): 9646–9662, https://doi.org/10.1007/s10853-021-06828-8

50. M. Sadaf, M. Bragaglia, and F. Nanni, "A Simple Route for Additive Manufacturing of 316L Stainless Steel via Fused Filament Fabrication," *Journal of Manufacturing Processes* 67 (2021): 141–150, https://doi.org/10.1016/j.jmapro.2021.04.055

51. N. Haghdadi, M. Laleh, M. Moyle, and S. Primig, "Additive Manufacturing of Steels: A Review of Achievements and Challenges," *Journal of Materials Science* 56 (2021): 64–107, https://doi.org/10.1007/s10853-020-05109-0

52. R. M. German, "Coarsening in Sintering: Grain Shape Distribution, Grain Size Distribution, and Grain Growth Kinetics in Solid-Pore Systems," *Critical Reviews in Solid State and Materials Sciences* 35 (2010): 263–305, https://doi.org/10.1080/10408436.2010.525197

53. J. Jansa, A. Volodarskaja, J. Hlinka, et al., "Corrosion and Material Properties of 316L Stainless Steel Produced by Material Extrusion Technology," *Journal of Manufacturing Processes* 88 (2023): 232–245, https://doi.org/10.1016/j.jmapro.2023.01.035

54. C. Gong, J. Marae Djouda, A. Hmima, et al., "Local Characterization of Stainless Steel 17-4PH Produced by Material Extrusion Additive Manufacturing: Influence of the Post-Treatment," *Materials Science and Engineering A* 880 (2023): 145371, https://doi.org/10.1016/j.msea.2023.145371

55. S. A. Tronvoll, N. P. Vedvik, C. W. Elverum, and T. Welo, "A New Method for Assessing Anisotropy in Fused Deposition Modeled Parts Using Computed Tomography Data," *International Journal of Advanced Manufacturing Technology* 105 (2019): 47–65, https://doi.org/10.1007/s00170-019-04081-7

56. D. Godec, S. Cano, C. Holzer, and J. Gonzalez-Gutierrez, "Optimization of the 3D Printing Parameters for Tensile Properties of Specimens Produced by Fused Filament Fabrication of 17-4PH Stainless Steel," *Materials (Basel)* 13 (2020): 774, https://doi.org/10.3390/ma13030774

57. G. H. Loh, E. Pei, J. Gonzalez-Gutierrez, and M. Monzón, "An Overview of Material Extrusion Troubleshooting," *Applied Sciences* 10 (2020): 10, https://doi.org/10.3390/app10144776

58. P. Bing, D. Wu, and Y. Xia, "Incremental Calculation for Large Deformation Measurement Using Reliability-Guided Digital Image Correlation," *Optics and Lasers in Engineering* 50 (2012): 586–592, https://doi.org/10.1016/j.optlaseng.2011.05.005

59. C. Tosto, J. Tirillò, F. Sarasini, and G. Cicala, "Hybrid Metal/Polymer Filaments for Fused Filament Fabrication (FFF) to Print Metal Parts," *Applied Sciences* 11 (2021): 1, https://doi.org/10.3390/app11041444

60. S. Mousavi, D. Howard, F. Zhang, J. Leng, and C. H. Wang, "Direct 3D Printing of Highly Anisotropic, Flexible, Constriction-Resistive Sensors for Multidirectional Proprioception in Soft Robots," *ACS Applied Materials & Interfaces* 12 (2020): 15631–15643, https://doi.org/10.1021/acsami.9b21816

61. W. Qin, J. Li, Y. Liu, et al., "Effects of Grain Size on Tensile Property and Fracture Morphology of 316L Stainless Steel," *Materials Letters* 254 (2019): 116–119, https://doi.org/10.1016/j.matlet.2019.07.058

62. S. Spiller and N. Razavi, *Investigation on the Tensile and Fatigue Properties of Small-Scale Specimens Fabricated With Material Extrusion Additive Manufacturing* (forthcoming).

63. N. P. Lavery, J. Cherry, S. Mehmood, et al., "Effects of Hot Isostatic Pressing on the Elastic Modulus and Tensile Properties of 316L Parts Made by Powder Bed Laser Fusion," *Materials Science and Engineering a* 693 (2017): 186–213, https://doi.org/10.1016/j.msea.2017.03.100

64. J. Kovacik, "Correlation Between Young's Modulus And Porosity in Porous Materials," *Journal of Materials Science* 18 (1999): 1007–1010.

65. M. Pellizzari, S. Furlani, F. Deirmina, R. Siriki, B. AlMangour, and D. Grzesiak, "Fracture Toughness of a Hot Work Tool Steel Fabricated by Laser-Powder Bed Fusion Additive Manufacturing," *Steel Research International* 91 (2020): 1–7, https://doi.org/10.1002/srin.201900449

66. P. Moore, "The Effect of Notch Sharpness on the Fracture Toughness Determined From SENT Specimens," in *Proceedings of the ASME 2014 33rd International Conference Ocean, Offshore and Arctic Engineering* (New York, NY: ASME, 2014), 1–7.

67. P. Lazzarin, F. Berto, M. Elices, and J. Gómez, "Brittle Failures From U- and V-Notches in Mode I and Mixed, I + II, Mode: A Synthesis Based on the Strain Energy Density Averaged on Finite-Size Volumes," *Fatigue and Fracture of Engineering Materials and Structures* 32 (2009): 671–684, https://doi.org/10.1111/j.1460-2695.2009.01373.x

68. N. Razavi, M. R. M. Aliha, and F. Berto, "Application of an Average Strain Energy Density Criterion to Obtain the Mixed Mode Fracture Load of Granite Rock Tested With the Cracked Asymmetric Four-Point Bend Specimens," *Theoretical and Applied Fracture Mechanics* 97 (2018): 419–425, https://doi.org/10.1016/j.tafmec.2017.07.004

69. L. Susmel, "The Theory of Critical Distances: A Review of Its Applications in Fatigue," *Engineering Fracture Mechanics* 75 (2008): 1706–1724, https://doi.org/10.1016/j.engfracmech.2006.12.004

70. L. Susmel and D. Taylor, "The Theory of Critical Distances as an Alternative Experimental Strategy for the Determination of $K_{Ic}$ and $\Delta K_{th}$," *Engineering Fracture Mechanics* 77 (2010): 1492–1501, https://doi.org/10.1016/j.engfracmech.2010.04.016

## Appendix I

### Application and Calibration of Theoretical Methods

#### I.1 | ASED Criterion

The ASED criterion is used to predict the failure conditions of notched components under static and fatigue loading. It was first formulated to deal with the failure of sharp V-notched components [42]. The basic idea is that the failure occurs when the strain energy density reaches a critical value. In the case of brittle linear elastic material, the critical value can be simply obtained as $W_c = \sigma_t^2 / 2E$, where $\sigma_t$ is the tensile strength and $E$ Young's modulus. At the tip of a sharp notch, the stress field, and therefore the strain energy density, tends to be infinite; hence, it is not possible to apply the criterion if only the tip point is considered. To solve the issue, it was thought to use a larger volume around the notch tip, where the total value of the strain energy is finite, calculating the ASED as total strain energy in the control volume over the control volume itself. The definition of the volume, which will be called control volume, was found to be dependent on the material properties and on the notch geometries. Indeed, the control volume has the shape of a circle centered on the crack tip in the case of physical cracks, with a tip radius of $\rho = 0$ and an opening angle of $2\alpha = 0$. For V-notches, the volume is reduced to a sector of a circle, depending on the opening angle of the notch, and finally, for the U-notches, the control volume assumes the shape of a crescent. The symmetry axis of the crescent is the notch bisector in the case of Mode I loading condition, while it rotates in the case of a mixed mode [67]. For all the possible notch geometries, the characteristic value to define is the control radius $R_c$, which requires the following material properties: $E$, $\nu$, $\sigma_t$, and $K_{Ic}$. There are different formulations based on the stress and strain field in the components. For plane strain problems, the equation reported in Figure A1a can be used. More details can be found in [43]. The failure criterion can be converted in terms of failure loads since the strain energy density depends on the stress intensity factors (squared), which are also calculated based on the load applied to the studied component. Hence, a proportionality between the applied load and ASED is established. In failure conditions, the applied load becomes the failure load, and the ASED reaches the critical value of $W_c$. The failure load can be calculated numerically, once $W_c$ and $R_c$ are defined. It is sufficient to model in an FE software a reference condition of the component under study, for example with only 1 N of applied load, and to calculate the ASED $\overline{W}$ as the ratio of strain energy and volume of the defined control volume. The prediction of the failure load $P_f$ is based on $P_f = P\sqrt{W_C / \overline{W}}$, as reported in [68].

In the case of the unavailability of accurate material properties, it might be useful to proceed with a calibration of the method [47]. The calibration consists of choosing different control volumes and calculating the corresponding strain energy density. In this way, the plot of the strain energy density vs. the control radius is obtained. Assuming the values of $W_c$ and $R_c$ are only material dependent, there must exist an intersection point in the $(\overline{W}; R)$ plots, common to all the possible notch geometries, that correspond to the critical values. It is suggested to consider two extreme conditions, for example, the sharpest and the bluntest notches available. This procedure was used, for example, in [32, 33, 47]. In the present work, models with notches ($\rho$) of 1 and 0.25 mm were used. The plot obtained is schematically represented in Figure A1a1. Once the critical values of strain energy density and control volume radius are defined, it is possible to proceed conventionally with the application of the criterion.

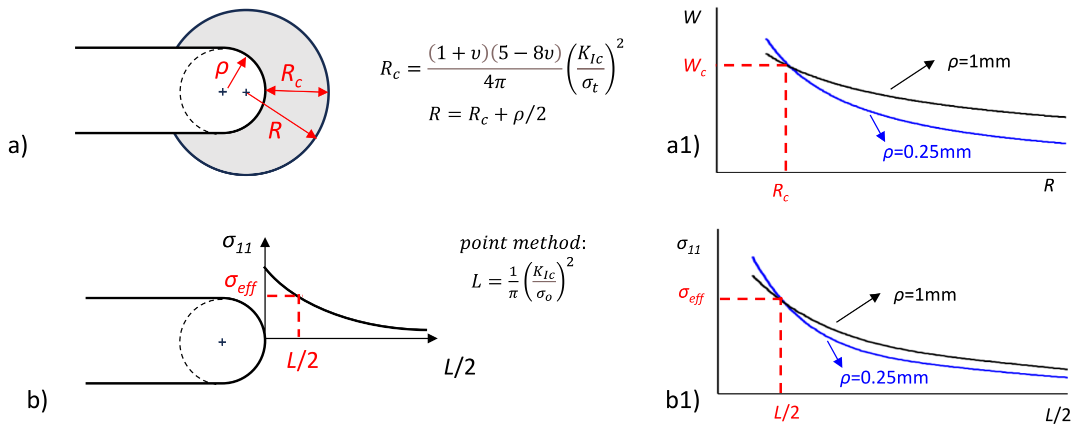


**FIGURE A1** | Schematics of the mechanisms and calibration procedures needed to apply the ASED criteria (a, a1) and the point method of the TCD (b, b1). [Colour figure can be viewed at wileyonlinelibrary.com]

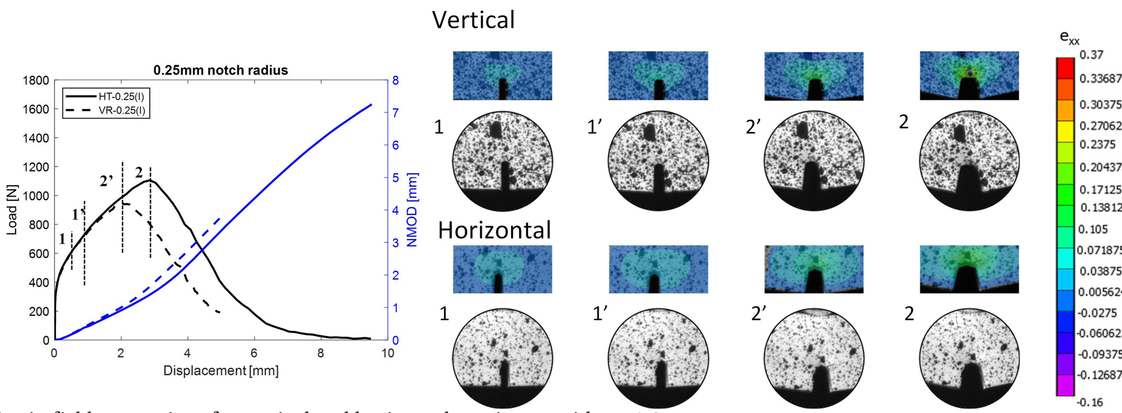


**FIGURE A2** Strain field comparison for vertical and horizontal specimens with $\rho = 0.25$ mm.

## I.2 | TCD

The TCD is another possible approach to predict the failure of notched components in static and fatigue loading [44]. It is indeed considered a family of methods since different applications can be implemented. Some of them are the so-called point method (PM), line method (LM), and area method (AM), although more variations exist [44, 69]. Independently of the method used, a length parameter called $L_c$ has to be calculated. The equation is shown in Figure A1b, and it requires the fracture toughness and the intrinsic tensile strength of the material $\sigma_{0.}$ This second parameter acts as an upper limit of the stress in the material; therefore, for brittle materials, it is often considered that $\sigma_0 = \sigma_t$. Each of the methods mentioned above also defined an effective stress $\sigma_{eff}$ that is supposed to reach the value of $\sigma_0$ in failure conditions. In the present work, the PM method has been used. The effective stress in this case is simply defined as equal to the maximum principal stress at a distance from the notch tip equal to $L_c/2$ along the notch bisector. This is considered an appropriate choice due to the loading condition of Mode I and the simplicity of the specimen's geometry. Alternatively, the equivalent stress field according to Tresca or Von Mises criteria can be used [28, 38].

The definition of inherent material strength for ductile materials as the 316L studied in the present work is less intuitive than for brittle or quasibrittle materials; therefore, a calibration procedure is suggested. The procedure, described in [28], resembles the one adopted to calibrate the critical values of the ASED criterion. The stress distributions of two different notched specimens are plotted as depicted in Figure A1b1. The intersection of the two trends allows us to define $\sigma_0$ and $L_c/2$ with $\sigma_0$, which is usually higher than the UTS of the material. Once the critical distance is defined, TCD methods can be applied. Moreover, TCD can be used backward, as in [70], in the definition of the fracture toughness of the material.

## Appendix II

### Notch Deformation Results via DIC

With the sole purpose of comparing horizontal and vertical specimens, the following strain fields are shown. It must be noted that such a microscopical characteristic is hard to capture in such small specimens that experience such a large deformation. Moreover, as was highlighted in the previous section, the speckle pattern painted on the specimen is quite coarse to accurately calculate the deformation. Nonetheless, the following pictures are reported. The portion of material invested by intense strain is generally larger in the horizontal specimen, but interestingly, the intensification is more acute at Point 2 in the vertical specimen. Indeed, at this point of the test, the horizontal specimen has barely reached the peak load, while the vertical present already signs of cracking from the notch.